Kinetic and functional analysis of transient, persistent and resurgent sodium currents in rat cerebellar granule cells *in situ*: an electrophysiological and modelling study

Jacopo Magistretti[1], Loretta Castelli[1], Lia Forti[1] and Egidio D'Angelo[1,2]

[1]*Dipartimento di Scienze Fisiologiche-Farmacologiche Cellulari-Molecolari, Sezione di Fisiologia Generale e Biofisica Cellulare, Università degli Studi di Pavia, Via Forlanini 6, 27100 Pavia, Italy*
[2]*Dipartimento di Biologia Evolutiva e Funzionale, Università degli Studi di Parma, Parco Area delle Scienze 11A, 43100 Parma, Italy*

Cerebellar neurones show complex and differentiated mechanisms of action potential generation that have been proposed to depend on peculiar properties of their voltage-dependent Na^+ currents. In this study we analysed voltage-dependent Na^+ currents of rat cerebellar granule cells (GCs) by performing whole-cell, patch-clamp experiments in acute rat cerebellar slices. A transient Na^+ current (I_{NaT}) was always present and had the properties of a typical fast-activating/inactivating Na^+ current. In addition to I_{NaT}, robust persistent (I_{NaP}) and resurgent (I_{NaR}) Na^+ currents were observed. I_{NaP} peaked at ∼−40 mV, showed half-maximal activation at ∼−55 mV, and its maximal amplitude was about 1.5% of that of I_{NaT}. I_{NaR} was elicited by repolarizing pulses applied following step depolarizations able to activate/inactivate I_{NaT}, and showed voltage- and time-dependent activation and voltage-dependent decay kinetics. The conductance underlying I_{NaR} showed a bell-shaped voltage dependence, with peak at −35 mV. A significant correlation was found between GC I_{NaR} and I_{NaT} peak amplitudes; however, GCs expressing I_{NaT} of similar size showed marked variability in terms of I_{NaR} amplitude, and in a fraction of cells I_{NaR} was undetectable. I_{NaT}, I_{NaP} and I_{NaR} could be accounted for by a 13-state kinetic scheme comprising closed, open, inactivated and blocked states. Current-clamp experiments carried out to identify possible functional correlates of I_{NaP} and/or I_{NaR} revealed that in GCs single action potentials were followed by depolarizing afterpotentials (DAPs). In a majority of cells, DAPs showed properties consistent with I_{NaR} playing a role in their generation. Computer modelling showed that I_{NaR} promotes DAP generation and enhances high-frequency firing, whereas I_{NaP} boosts near-threshold firing activity. Our findings suggest that special properties of voltage-dependent Na^+ currents provides GCs with mechanisms suitable for shaping activity patterns, with potentially important consequences for cerebellar information transfer and computation.

(Resubmitted 1 February 2006; accepted after revision 1 March 2006; first published online 9 March 2006)
Corresponding author J. Magistretti: Dipartimento di Scienze Fisiologiche-Farmacologiche Cellulari-Molecolari, Sezione di Fisiologia Generale e Biofisica Cellulare, Università degli Studi di Pavia, Via Forlanini 6, 27100 Pavia, Italy. Email: jmlab1@unipv.it

Granule cells (GCs) are small neurones that occupy a key position within the cerebellar-cortex circuitry forming the input layer of the major cerebellar afferent system. Mossy fibres activate GCs, which emit their output to other neurones in the cerebellar cortex through parallel fibres. In turn, GCs receive feed-forward and feed-back inhibition from Golgi cells (Eccles *et al.* 1967). Understanding the mechanisms that regulate GC action potential (AP) discharge upon excitation is particularly important, since GCs determine the AP code to be relayed into the cerebellar circuitry.

Voltage-dependent Na^+ currents appear to play an important role in regulating the intrinsic activity patterns expressed by cerebellar neurones. Current-clamp recordings in acute cerebellar slices (D'Angelo *et al.* 1995, 1998; Brickley *et al.* 1996) and *in vivo* (Chadderton *et al.* 2004) have shown that GCs behave as regular spiking neurones in response to sustained, intense depolarizing stimuli. In the presence of just-threshold depolarization, however, GCs also show additional, peculiar patterns of activity and AP organization (D'Angelo *et al.* 1998, 2001). Single APs are preceded by slow, ramp-like

 DOI: 10.1113/jphysiol.2006.106682

depolarizing prepotentials, and are often followed by transient depolarizing afterpotentials (DAPs) that may also recur a few times before the subsequent AP is fired. APs are not regularly spaced, but tend to cluster into low-frequency bursts. It was suggested that prepotentials, DAPs and spike clustering reflect the intervention of a persistent Na^+ current (I_{NaP}; D'Angelo *et al.* 1998), similar to I_{NaP} that in various neurones subtend sub- and near-threshold sustained depolarizing events (discussed in Magistretti & Alonso, 2002). Indeed, in the presence of K^+- and Ca^{2+}-channel block, the steady-state voltage-current (V–I) relationship of GCs shows an inward rectification region at about −55 to −30 mV that is abolished by tetrodotoxin (TTx) (D'Angelo *et al.* 1998). Modelling data also support the notion that the depolarizing envelope subtending AP bursts depends on I_{NaP} (D'Angelo *et al.* 2001). In addition, a resurgent Na^+-current component (I_{NaR}; Raman & Bean, 1997) has recently been demonstrated in GCs (Magistretti *et al.* 2004; Afshari *et al.* 2004), and has also been suggested to participate in GC AP clustering (D'Angelo *et al.* 2001). I_{NaR} activates upon repolarization after depolarizations able to fully inactivate the transient Na^+ current (I_{NaT}), and corresponds to Na^+ channels transiently dwelling in the open state during return to closed states (Raman & Bean, 2001). In Purkinje cells, where it was first described, I_{NaR} has been proposed to promote the discharge of doublets or triplets of APs, instead of single spikes, in response to brief depolarizing pulses (Raman & Bean, 1997), thus contributing to AP conglomeration. In Purkinje cells, I_{NaR} also appears to have a role in enhancing firing frequency during tonic discharge (Khaliq *et al.* 2003). A similar role could also be played by I_{NaR} in GCs, which can produce relatively high maximal firing frequencies (120–150 Hz) (D'Angelo *et al.* 1998; Chadderton *et al.* 2004).

The above findings underscore the importance of determining the biophysical and functional properties of voltage-dependent Na^+ currents (VDNCs) expressed by native GCs, and especially of those active in the sub- and near-threshold range of membrane potentials. Because a detailed analysis of VDNCs in native GCs is still lacking, in the present work we have carried out a thorough characterization of VDNCs in GCs *in situ* by performing whole-cell patch-clamp experiments in rat cerebellar slices. Besides I_{NaT}, persistent and resurgent Na^+ currents were observed. We provide a biophysical characterization for each of these Na^+-current components. We also present current-clamp and modelling data suggesting that I_{NaR} is involved in generating DAPs and enhances high-frequency firing, whereas I_{NaP} controls near-threshold firing activity, thus contributing to set the excitable properties of these neurones.

Methods

The animal experiments described in the manuscript conformed with the rules established by the University of Pavia for the use of animals in experimental studies, in compliance with the guidelines of the Italian Ministry of Health, the national laws on animal research (d.l. 116/92), and the EU guidelines on animal research (N. 86/609/CEE).

Slice preparation

Young Wistar rats (16–23 days old) were anaesthetized by inhalation of alothane (Sigma-Aldrich, Milan, Italy) and decapitated. The cerebellum was quickly extracted under hypothermic conditions and submerged in an ice-cold dissection Krebs solution composed of (mmol l^{-1}): 127 NaCl, 1.32 KCl, 26 $NaHCO_3$, 1.18 KH_2PO_4, 1.19 $MgSO_4$, 0.2 ethyleneglycol-bis-(β-aminoethyl ether)*N*,*N*,*N*′,*N*′-tetraacetic acid (EGTA), 16 D-glucose (pH 7.4 by saturation with 95% O_2, 5% CO_2). The cerebellar vermis was isolated from the hemispheres and blocked on the stage of a Microslicer DTK-1000 vibratome (Dosaka, Kyoto, Japan) using cyanoacrylate glue. During the sectioning procedure the tissue was submerged in an ice-cold (∼1–2°C) cutting solution containing (mmol l^{-1}): 130 potassium gluconate, 15 KCl, 20 *N*-2-hydroxyethylpiperazine-*N*′-2-ethanesulphonic acid (Hepes), 0.2 EGTA, 11 D-glucose (pH 7.4 with KOH). Using this high-K^+ solution was found to improve neurone viability (Stéphane Dieudonné, unpublished results). Sagittal sections (250 μm thick) were cut, then rinsed in maintenance Krebs solution containing (mmol l^{-1}): 127 NaCl, 1.32 KCl, 26 $NaHCO_3$, 1.18 KH_2PO_4, 1.19 $MgSO_4$, 2 $CaCl_2$, 11 D-glucose (pH 7.4 by saturation with 95% O_2, 5% CO_2), and transferred to an incubation chamber filled with the same solution (continuously bubbled with 95% O_2, 5% CO_2). The slices were kept submerged in the incubation chamber at room temperature for at least 1 h before starting the recording.

Patch-clamp experiments: voltage-clamp recordings

The recording chamber was mounted on the stage of an inverted microscope (Axiovert 100; Zeiss, Oberkochen, Germany). Slices were transferred, one at a time, to the chamber and perfused with a solution suitable for isolating Na^+ currents, containing (mmol l^{-1}): 100 NaCl, 26 $NaHCO_3$, 19.5 tetraethylammonium chloride (TEA-Cl), 3 KCl, 2 $MgCl_2$, 2 $CaCl_2$, 2 $BaCl_2$, 0.5 $CdCl_2$, 4 4-aminopyridine, 11 D-glucose (pH 7.4 by saturation with 95% O_2, 5% CO_2). The perfusion rate was about 1 ml min^{-1}. Patch pipettes were fabricated from thick-wall borosilicate glass capillaries (CEI GC 150–7.5; Harvard Apparatus, Edenbridge, UK) by means of a Sutter P-87 horizontal puller (Sutter Instruments, Novato, CA, USA). The pipette solution contained (mmol l^{-1}): 104 CsF, 50 TEA-Cl, 2 $MgCl_2$, 10 Hepes, 10 EGTA, Na_2ATP, and 0.2 NaGTP (pH adjusted to 7.2 with CsOH). The patch pipettes had a resistance of 5–8 MΩ when filled with the above solution. The recording electrode was inserted into

the granular layer of the slice after application of positive pressure, and approached blindly to neurones *in situ* as described elsewhere (D'Angelo *et al.* 1993). Tight seals (>10 GΩ) and the whole-cell configuration were obtained by suction.

Voltage-clamp recordings of Na^+ currents were performed at room temperature (21–24°C) by means of an EPC7 patch-clamp amplifier (List Electronics, Darmstadt, Germany). Series resistance (R_s) was continually monitored during the experiment using the amplifier built-in compensation section, and always compensated by 50–70% (average value, 55.5%; $n = 128$). Recordings in which R_s levels varied with time by more than 2 MΩ were discarded. Voltage protocols were commanded and current signals were acquired with a Pentium personal computer interfaced to a Tl–1 interface (Axon Instruments, Union City, CA, USA) using program Clampex of the pClamp 6.0.5 software package (Axon Instruments). In all recordings the holding potential was −80 mV. Current signals were low-pass filtered and digitized at different frequencies according to the experimental protocol applied: cut-off and sampling frequencies were 5 and 50 kHz, respectively, for I_{NaT} activation protocols and I_{NaR} protocols; 5 and 20 kHz, respectively, for I_{NaT} steady-state inactivation protocols and I_{NaP} 500 ms step protocols; 2 and 5–10 kHz, respectively, for ramp protocols. Currents were always on-line leak subtracted via a P/4 routine, except in the case of protocols applied for I_{NaP} study (see Fig. 3).

Tetrodotoxin (TTx; Alomone Laboratories, Jerusalem, Israel) was applied in the bath with the superfusing solution.

Patch-clamp experiments: current-clamp recordings

Current-clamp recordings were obtained from GCs in cerebellar slices. Slices were perfused with a solution containing (mmol l^{-1}): 120 NaCl, 2 KCl, 1.2 $MgSO_4$, 26 $NaHCO_3$, 1.2 KH_2PO_4, 2 $CaCl_2$, 11 D-glucose, 1 kynurenic acid, 0.1 picrotoxin (pH 7.4 by saturation with 95% O_2, 5% CO_2). The pipette solution contained (mmol l^{-1}): 135 or 145 potassium gluconate, 5 KCl, 10 Hepes, 0.2 EGTA, 4.6 $MgCl_2$, 2 Na_2ATP, 0.4 NaGTP, pH 7.35. Recordings were performed at room temperature using a Multiclamp amplifier or an Axopatch 200B amplifier (both from Axon Instruments), the latter being used in the I_{fast} mode. Clampex 8.2 and a Digidata 1322A digitiser were used to inject current steps and acquire voltage signals. Sampling frequency was 50 kHz. No R_s compensation (bridge balance) was used. Voltage measurements were not corrected for errors introduced by R_s (≤1 mV).

Data analysis

Whole-cell current and voltage signals were analysed by means of program Clampfit of pClamp 6.0.5 and pClamp 8.2, respectively. Na^+ currents were normally re-filtered off-line at 2–3.5 kHz. Current amplitude was measured at the peak of each tracing, unless otherwise specified. Na^+ permeabilities (P_{Na}) were calculated from current amplitudes (I_{Na}) by applying the Goldman-Hodgkin-Katz equation in the form:

$$P_{Na} = I_{Na}\left(RT/F^2V_m\right)[1 - \exp(-FV_m/RT)]/\{[Na^+]_i - [Na^+]_o \exp(-FV_m/RT)\} \quad (1)$$

in which the nominal intra- and extracellular Na^+ concentration values (4.2 and 126 mM, respectively) were introduced.

To analyse I_{NaT} time course according to a Hodgkin-Huxley (HH) formalism, exponential fittings of I_{NaT} inactivation phase were first carried out. Second-order exponential functions were consistently required for proper fitting at test potentials of −35 to +15 mV. Because in the HH model the activation and inactivation processes are independent, current tracings were divided by their inactivation fitting functions, extrapolated to time zero of the depolarizing test pulse, to reconstruct the time course of the HH activation process. The curves thus obtained were then fitted with a HH activation function in the form:

$$y = m(t)^n = [1 - \exp(-t/\tau_m)]^n \quad (2)$$

where the power coefficient n was either left free to vary or kept at a fixed value (see Results).

Data fittings with exponential functions, $I = \Sigma A_i \exp(-t/\tau_i) + C$, were carried out using Clampfit. Fittings with Boltzmann functions, $y = y_{max}/\{1 + \exp[(V - V_{½})/k)]\}$, and HH activation functions (see above) were carried out using Origin 6.0 (OriginLab Corp., Northampton, MA, USA).

R_s was evaluated off-line by analysing the properties of capacitive current transients evoked by −10 mV voltage square pulses from the holding potential of −80 mV, as explained elsewhere (D'Angelo *et al.* 1993). Average R_s was 27.9 ± 1.2 MΩ ($n = 84$).

Average values are expressed as means ± S.E.M. Statistical significance was evaluated by means of a two-tail Student's t test for paired or unpaired data.

Computer simulations

Computer simulations of GC electrical activity were performed in the NEURON environment (Hines & Carnevale, 1997) by employing a GC single-compartment model described in detail elsewhere (D'Angelo *et al.* 2001). Modelling schemes and kinetic parameters were identical to those described in D'Angelo *et al.* (2001) for all membrane currents except Na^+ currents. The HH-type formalism, previously employed to separately model I_{NaT}, I_{NaP} and I_{NaR}, was replaced with the 13-state, allosteric

Na^+-channel model by Raman & Bean (2001) in the modified form described by Khaliq *et al.* (2003), which simultaneously generates the three current components, and is shown in Scheme 1.

It is worth remarking that the model implicitly assumes the existence of a single Na^+ channel accounting for all Na^+-current components. The values of the kinetic parameters in Scheme 1 were adjusted to fit the observed properties of all Na^+-current components, and were set as follows: $\alpha = 353.9 \exp(V/k_\alpha)\ ms^{-1}$, $\beta = 1.272 \exp(-V/k_\beta)\ ms^{-1}$, $k_\alpha = k_\beta = 13.9$ mV, $n_1 = 5.42$, $n_2 = 3.28$, $n_3 = 1.83$, $n_4 = 0.74$; $\gamma = 150\ ms^{-1}$, $\delta = 40\ ms^{-1}$, $\varepsilon = 1.75\ ms^{-1}$, $\zeta = 0.0201 \exp(-V/k_\zeta)\ ms^{-1}$, $k_\zeta = 25.0$ mV; $C_{on} = 0.005\ ms^{-1}$, $C_{off} = 0.5\ ms^{-1}$, $O_{on} = 0.75\ ms^{-1}$, $O_{off} = 0.005\ ms^{-1}$, $a = (O_{on}/C_{on})^{1/4}$, $b = (O_{off}/C_{off})^{1/4}$. Na^+ current was calculated as: $I_{Na} = f\overline{G}_{Na}(V - V_{Na})$, where f is the fraction of channels in the open (O) state as returned by numerical resolution of Scheme 1 for time and voltage; $\overline{G}_{Na}$, the maximal Na^+ conductance, was 8.0 mS cm^{-2}; and V_{Na}, the Na^+ equilibrium potential, was +87.4 mV.

To modify the persistent or the resurgent current components, kinetic constants were modified as follows: (1) I_{NaR} was switched off by setting the forward rate constant for the O → OB transition, ε, to zero. By itself, this modification ('0-I_{NaR}^- condition', for brevity) also resulted in considerable slowing of I_{NaT} decay (see Fig. 8*C*, violet tracing), due to the lack of the O → OB transition, which is a major exit path from the open state. (2) With ε set at zero, the rate constant of the O → I6 transition, O_{on}, was increased to 2.15 ms^{-1} to restore the normal I_{NaT} decay speed. At the same time, the rate constant of the I6 → O transition, O_{off}, was increased to 0.01433 ms^{-1} to prevent reduction of the persistent component. These changes ('0-I_{NaR}^+ condition', for brevity) allowed us to obtain Na^+ currents in which the I_{NaR} component was absent while the I_{NaT} and I_{NaP} components were largely unmodified (see Fig. 8*C* and *D*, red tracings). Note that the 0-I_{NaR}^+ condition can be regarded as the equivalent of endowing the cell with a set of Na^+ currents identical to control currents, with the only difference of I_{NaR} absence, whereas the 0-I_{NaR}^- condition can be viewed as the equivalent of removing the mechanism of I_{NaR} generation with no additional re-adjustments. (3) To reduce the steady-state I_{NaP} in the absence of other changes, the rate constant of the I6 → O transition, O_{off}, was decreased to 0.002 or 0.0015 ms^{-1} (all other kinetic parameters were left unmodified). This resulted in an I_{NaP} reduction of 58 or 67%, respectively, at the steady state.

All other membrane parameters of the GC model, including specific membrane conductances, membrane surface area, and ion equilibrium potentials, as well as all parameters related to intracellular-Ca^{2+} dynamics, were the same as specified in D'Angelo *et al.* (2001). In both simulated voltage-clamp and current-clamp experiments, temperature was set at 22°C.

Results

Voltage-clamp experiments were performed under ionic conditions suitable to isolate Na^+ currents (see Methods). Current tracings recorded in the presence of 1 μM TTx were routinely subtracted from control tracings to better isolate TTx-sensitive Na^+ currents from contaminants. Recordings on GCs *in situ* were obtained from cells located in the external part of cerebellar lobules VI–IX. These experiments allowed us to identify three distinct Na^+-current components in GCs.

Transient Na^+ current

Transient Na^+ currents (I_{NaT}) were studied by delivering 20 ms voltage square pulses at −75 to +20 mV in 5 mV increments. This depolarizing protocol elicited I_{NaT} that were always abolished by 1 μM TTx (Fig. 1*A* and *B*). In a large majority of GCs *in situ* (for brevity, named group 1 cells, $n = 60$ out of 84) I_{NaT}s showed signs of poor space clamp control (Fig. 1*A*). These currents included an unclamped component that was activated starting from −60 to −45 mV, typically after a more or less pronounced lag, and showed virtually no increase in amplitude in the subsequent one or two depolarizing steps. At more positive voltages a better-clamped component

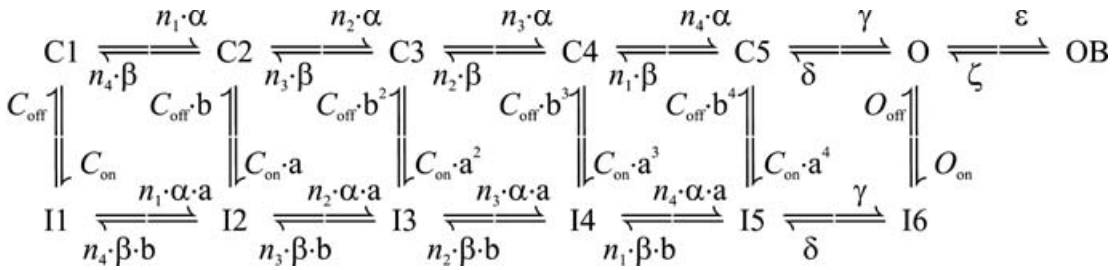

Scheme 1

superimposed to the unclamped component, suggesting that in these cells the Na^+ current was due to channels located partly in a membrane region electrotonically distant from the soma (presumably the axon), and partly in a more proximal region. In a few other cells (group 2, $n = 12$), the second, well-clamped Na^+-current component was observed in isolation: an example of the currents recorded in these neurones is illustrated in Fig. 1*Ba*. In the remaining 12 cells, either currents with features intermediate between those of the two other groups ($n = 6$) or fully unclamped spikes ($n = 6$) were observed. Only the currents recorded in group 2 cells were used for the study of I_{NaT} biophysical properties. In group 2 cells, a measurable I_{NaT} was activated starting around

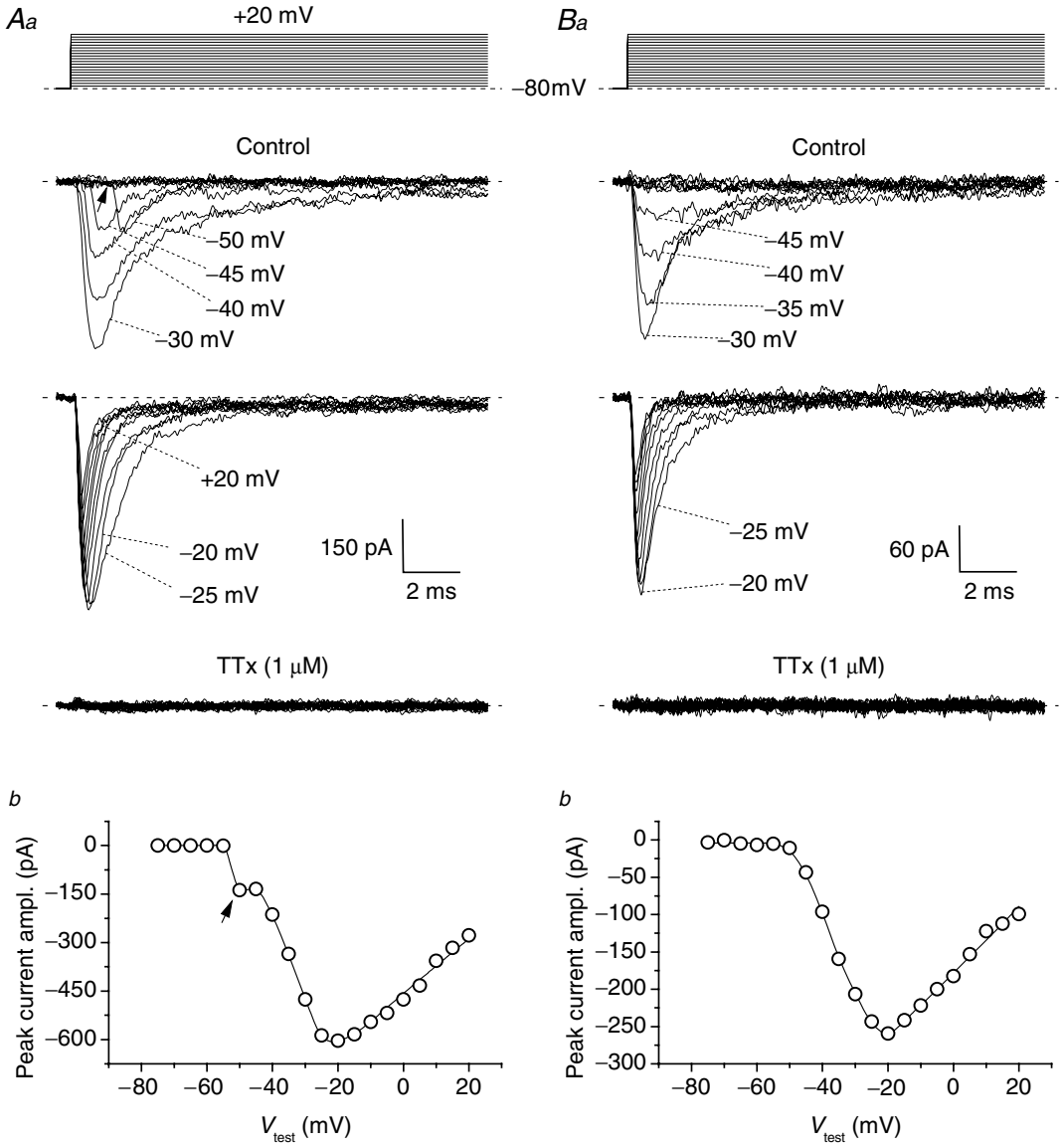

Figure 1. Transient Na^+ currents (I_{NaT}) in granule cells (GCs) *in situ*
A and *B*, the properties of the I_{NaT} recorded in two typical GCs (cell C4120 in *A*, and cell C4129 in *B*, representative of 60 and 12 cells, respectively). The voltage-clamp protocol applied to activate I_{NaT} is shown in the upper part of *Aa* and *Ba*. The middle part of the panels shows the experimental tracings thus obtained in control conditions (the tracings recorded at −75 to −30 mV, and at −25 to +20 mV, have been split in two different subpanels). The lower part of the panels shows the tracings recorded in the presence of 1 μM tetrodotoxin (TTx). *Aa*, example of the currents recorded in group 1 neurones (see the text), in which an unclamped and a well-clamped I_{NaT} component were apparent. The arrow points to the prominent lag preceding the activation of the unclamped component at its threshold. *Ba*, example of the currents recorded in group 2 neurones (see the text), in which the well-clamped I_{NaT} component was observed in isolation. *Ab* and *Bb*, current–voltage (*I–V*) relationships for I_{NaT} peak amplitude in the same two cells.

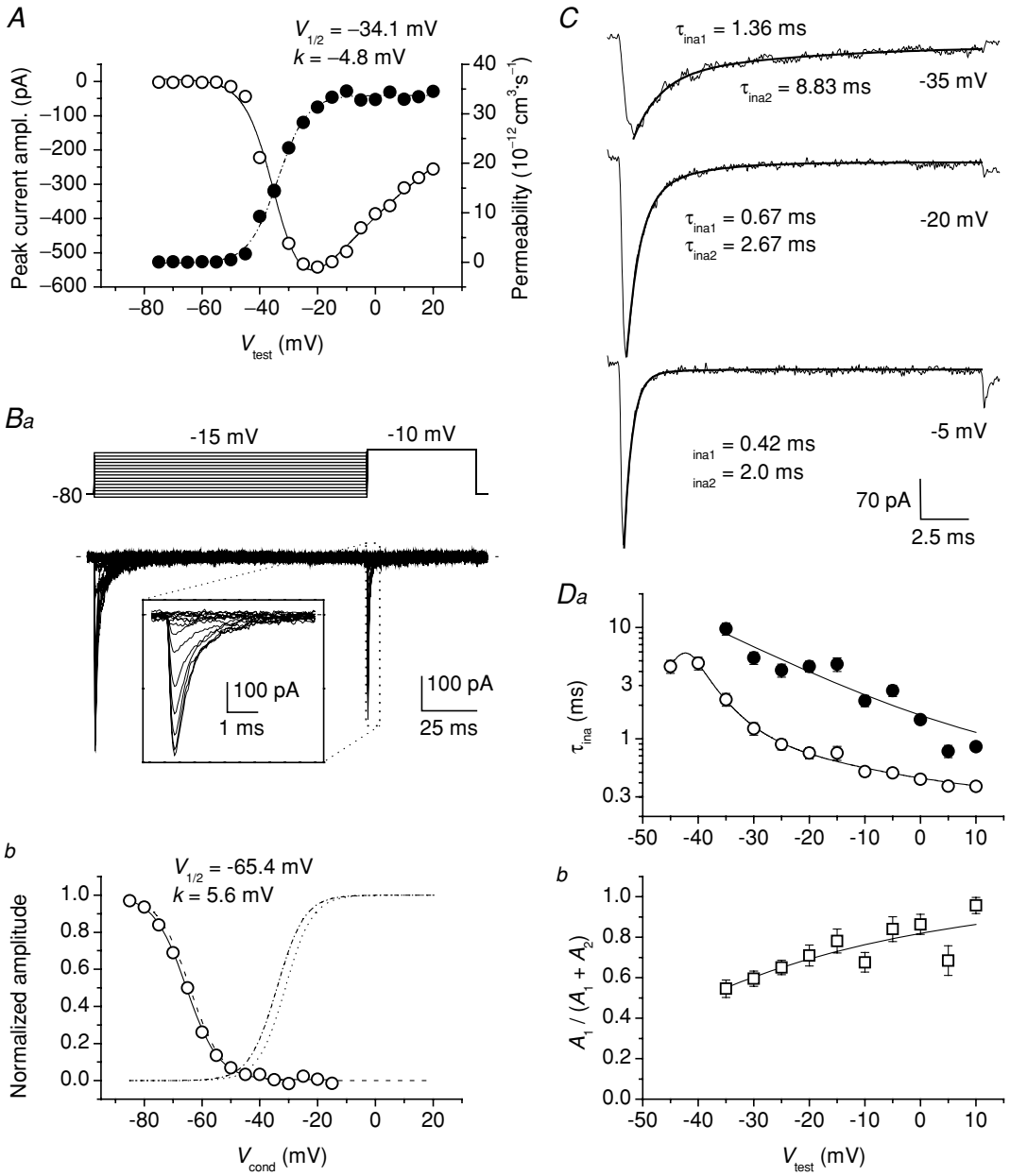

Figure 2. I_{NaT} in GCs: voltage dependence of activation, steady-state inactivation, and kinetics
A, average, normalized (*I–V*) relationship of I_{NaT} in a representative group 2 GC (cell B3512) (○), and the corresponding permeability values (P_{NaT}, calculated as explained in Methods), plotted as a function of test potential, V_{test} (●). The P_{NaT}–*V* plot was best-fitted with a single Boltzmann function (dashed–dotted line): the fitting parameters thus obtained are also specified. The continuous line has been obtained from the same fitting function by converting permeability into current on the basis of the Goldman-Hodgkin-Katz (GHK) equation. *Ba*, voltage-clamp protocol applied to study I_{NaT} steady-state inactivation (top), and the currents thus obtained in the same cell illustrated in *A* (bottom). The duration of the conditioning prepulse was 125 ms. The inset shows a detail, over an expanded time scale, of the currents elicited by the activating pulse. *Bb*, plot of voltage dependence of I_{NaT} steady-state inactivation for the same cell. The peak amplitude values of the currents elicited by the activating pulse of the protocol illustrated in *Ba* were normalized for the maximal value observed and plotted as a function of conditioning-prepulse potential, V_{cond} (○). The continuous line is the best Boltzmann fitting to data points; fitting parameters are also specified. The activation P_{NaT}–*V* function obtained for this cell, normalized to its asymptotic value, is shown for comparison (dashed–dotted line: same as in *A*). The dotted line and the dashed line are average activation and steady-state inactivation functions, respectively, constructed as Boltzmann functions in which parameters $V_{1/2}$ and k equalled the respective average values (see the text). *C*, three exemplary I_{NaT} tracings recorded at the test potentials of −35, −20 and −5 mV in a representative group 2 GC (cell B4203).

−50 mV and the current-voltage (*I–V*) relationship peaked at −20/−15 mV (Figs 1*Bb* and 2*A*, open circles), with I_{NaT} amplitude at the *I–V* peak averaging -446.3 ± 74.9 pA ($n = 12$) (in group 1 cells, peak I_{NaT} amplitude was -640.3 ± 40.3 pA, $n = 60$). Peak current–amplitude values were used to calculate the permeability underlying I_{NaT} (P_{NaT}) as explained in the Methods, and P_{NaT} values were plotted as a function of test potential (Fig. 2*A*, filled circles). The P_{NaT}–*V* plots obtained were fitted with a Boltzmann function, which returned an average half-maximal activation potential ($V_{½}$) of -31.2 ± 1.9 mV and an average activation slope factor (k) of -4.7 ± 0.3 mV ($n = 12$). A steady-state inactivation protocol (Fig. 2*Ba*) was also routinely applied, and the results were analysed in group 2 cells (Fig. 2*Bb*): Boltzmann fitting of steady-state inactivation plots returned average $V_{½}$ and k values of -64.2 ± 3.6 mV and $+5.5 \pm 0.2$ mV, respectively, ($n = 5$).

I_{NaT} kinetics was also analysed in group 2 cells. I_{NaT} inactivation was first examined. The current inactivation phase was best described by a second-order exponential function at −35 to +15 mV (Fig. 2*C*). Both the fast and slow exponential components strongly accelerated with depolarization, as shown by the plot of the two inactivation time constants (τ_{ina1} and τ_{ina2}) as a function of test potential (V_{test}) (Fig. 2*Da*). In addition, the relative weight of the fast exponential component tended to increase with depolarization (Fig. 2*Db*). I_{NaT} activation kinetics was then analysed by either considering rise time from 10 to 90% of peak amplitude (RT_{10-90}) or performing HH fittings of the current waveform (see Methods). RT_{10-90} decreased from an average value of 1.3 ms at −45 mV to 155 μs at −10 to +10 mV (not shown). The application of the HH fitting procedure revealed that when n, the power coefficient of the HH fitting function (Methods, eqn. (2)), was treated as a free fitting parameter, its value varied considerably at different V_{test} values, and markedly increased with depolarization (from ∼2 at −45/−40 mV to ∼9 at +5/+10 mV; see Supplemental Fig. A). Fixing the value of n at 4 or, even more, 3, returned a poorer correspondence of fittings with experimental tracings. The time constant of activation, τ_m, clearly tended to decrease with depolarization in HH fittings performed with free n (from 350 μs at −45/−40 mV to 65 μs at +5/+10 mV; Supplemental Fig. A, panel B1) and also, although to a lesser extent, with fixed n.

To evaluate the influence of series-resistance errors on the above measurements, we calculated the maximal estimated voltage error due to series resistance as $V_{err}(\max) = R_s(1 - f_{comp})I_{NaT}(\max)$, where R_s is series resistance, f_{comp} is the fraction of R_s compensation, and $I_{NaT}(\max)$ is the maximal Na^+-current amplitude. In group 2 neurones, $V_{err}(\max)$ averaged 4.9 ± 0.9 mV ($n = 12$).

Persistent Na^+ current

The application of long-lasting depolarizing steps and slow depolarizing ramps revealed that GCs *in situ* express, in addition to I_{NaT}, a small non-inactivating Na^+-current component. Examples of such a persistent Na^+ current (I_{NaP}) are illustrated in Fig. 3. Both group 1 and group 2 cells were considered for the study of I_{NaP}. The I_{NaP} evoked by 500 ms depolarizing pulses at −75 to −15 mV, in 5 mV increments, was first characterized (Fig. 3*Ab*). The application of this protocol revealed the presence of I_{NaP} as a sustained, TTx-sensitive inward-current component (Fig. 3*Ab*, lower tracings). Because of the very small size of this current, its properties were analysed after averaging experimental tracings obtained from a number of different cells, which substantially increased the signal-to-noise ratio and the reliability of measurements (Fig. 3*B*). The cells used to obtain the average current (10 group 1 cells plus 5 group 2 cells) were selected on the sole basis of optimal input-resistance and holding-current stability. I_{NaP} started to activate at about −65 mV, and its peak was at about −40 mV (Fig. 3*C*). The absolute amplitude of the average I_{NaP} (derived by considering the data points between 400 and 500 ms from the pulse onset) was −9.1 pA at the peak of the *I–V* relationship, which corresponds to 1.54% of the average maximal I_{NaT} amplitude observed in the same cells (-589.3 ± 82.9 pA, $n = 15$). The voltage dependence of the permeability underlying the average I_{NaP} (P_{NaP}) is also shown in Fig. 3*C* (filled circles). Boltzmann fitting to data points returned $V_{½}$ and k values of −55.3 mV and −4.7 mV, respectively.

In order to quickly explore the whole voltage range of I_{NaP} activation, slow ramp protocols able to inactivate I_{NaT} were also used. Ramp depolarizations from −80 to +20 mV at 100 mV s^{-1} evoked currents that, after TTx subtraction, provided a continuous *I–V* relationship for I_{NaP} (Fig. 3*D* and *E*). The *I–V* relationships thus obtained showed a 'threshold' at −70/−60 mV and a peak at about −40 mV (Fig. 3*E*). P_{NaP}–*V* plots were also derived from ramp-activated currents and fitted with single Boltzmann functions, which returned $V_{½}$ and k values very similar to those obtained from the analysis of step protocols (Fig. 3*F*). We also found that if the ramp slope was decreased

The inactivation phase of each current tracing has been best-fitted with a double exponential function (thick lines): the values of the fast and the slow inactivation time constants (τ_{ina1} and τ_{ina2}, respectively) are also specified. *D*, plots of average I_{NaT} inactivation time constants (*Da*; ○ and ●: τ_{ina1} and τ_{ina2}, respectively) and relative amplitude of the fast exponential component (*Db*) as a function of V_{test} ($n = 12$). Note the logarithmic scale of the *y*-axis in *Da*.

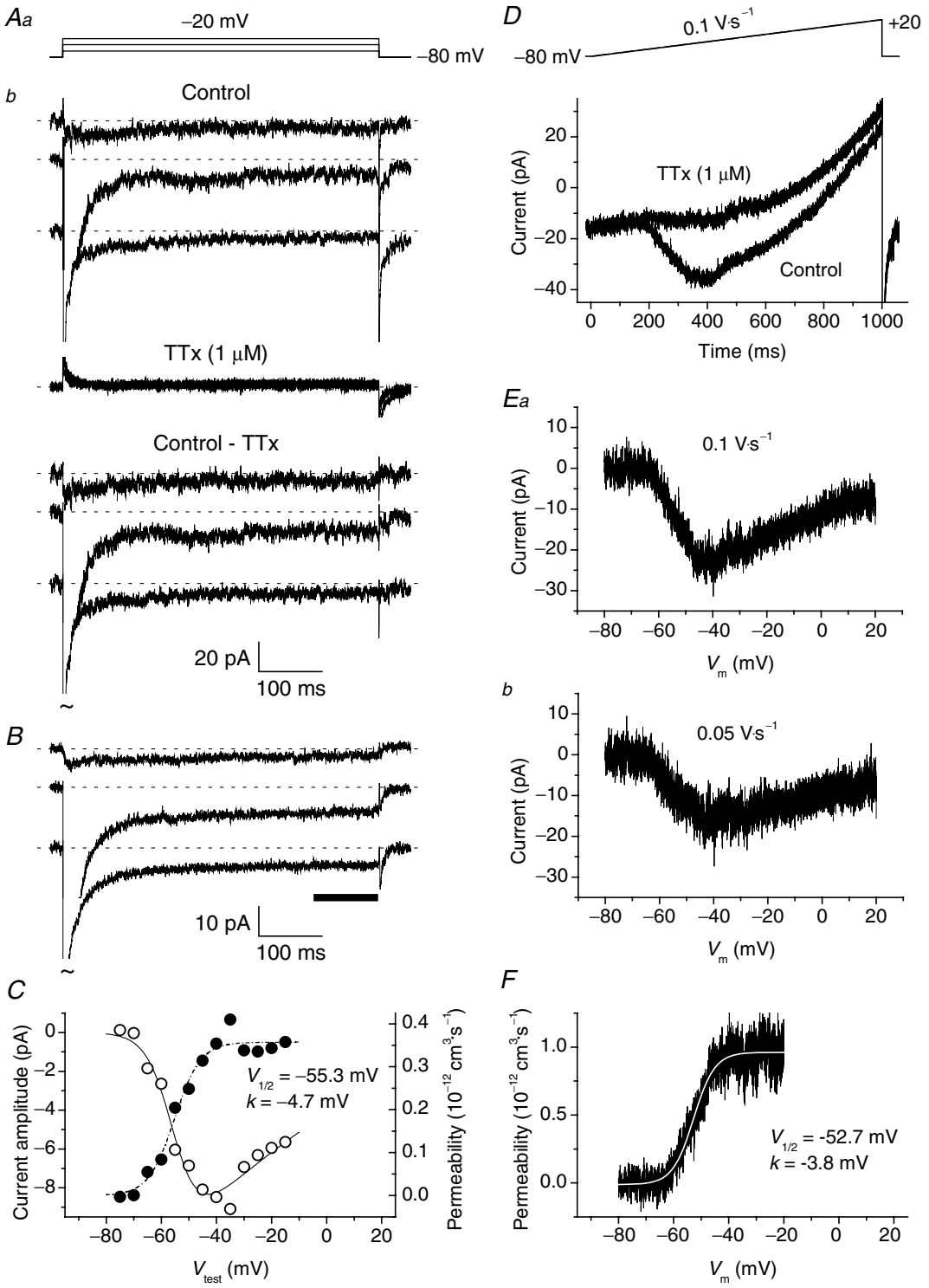

Figure 3. Persistent Na^+ current (I_{NaP}) GCs

I_{NaP} was activated by long-lasting step depolarizations (*A*–*C*) or ramp protocols (*D*–*F*). *A*, selected tracings from a representative GC (cell C3328). The current tracings shown in *Ab* have been recorded, in control conditions and in the presence of 1 μM TTx, in response to the voltage pulses illustrated in *Aa*. In this depolarizing-step protocol, the P/4 leakage subtraction routine was disabled to reduce background noise, and Na^+ currents were isolated from capacitive and leakage currents and other contaminants via TTx subtraction. TTx-sensitive currents are shown in the lower part of *Ab*. Tildes indicate that I_{NaT} peaks have been truncated. *B*, average, TTx-subtracted current tracings obtained from 15 different neurones. The voltage protocol applied was the same as illustrated in *Aa* (test potentials are, from top to bottom, −60, −40 and −20 mV). The horizontal bar indicates the region of each tracing

to 50 mV s^{-1}, the resulting I_{NaP} had a peak amplitude significantly lower than observed with 100 mV s^{-1} ramps (-15.1 ± 2.4 *versus* -22.4 ± 3.4 pA, respectively; $n = 29$; $P < 1 \times 10^{-4}$, *t* test for paired data) (Fig. 3*E*), which suggests the existence of slow I_{NaP} inactivation during sustained depolarizations (see Discussion).

Resurgent Na^+ current

The application of repolarizing pulses after I_{NaT} activation and decay led, in most GCs *in situ*, to activation of a resurgent Na^+ current (I_{NaR}). Figure 4*A* shows the currents recorded in a representative cell in response to a voltage-clamp protocol consisting of a 20 ms step pulse at 0 mV that activated I_{NaT}, followed by a 100 ms pulse at −40 mV. The repolarizing pulse induced an extra inward current that activated and then decayed in a time-dependent manner, and was abolished by 1 μM TTx. This current was therefore identified as I_{NaR}. Both group 1 and group 2 cells were considered for the study of I_{NaR}. The presence of space-clamp problems, reported in group 1 cells by poor clamp control of part of I_{NaT}, is unlikely to significantly affect I_{NaR}, due to the relatively slow time course of this current component.

Although the majority of GCs expressed a measurable I_{NaR}, the current size was usually small, making its analysis problematic in individual cells. Therefore, average tracings from recordings made in different cells were constructed and used to perform an accurate analysis of I_{NaR} biophysical properties. A set of average tracings derived from six different GCs (4 group 1 cells, 2 group 2 cells) is shown in Fig. 4*B*. I_{NaR} was routinely elicited by commanding repolarizing pulses at −15 to −85 mV in 5 mV steps. Figure 4*B* (bottom) illustrates the currents evoked at 10 mV intervals. Several lines of evidence indicate that these currents were not merely tail currents due to current flow through non-inactivated Na^+ channels (responsible for I_{NaP}): (1) peak current amplitude increased and then decreased as the level of repolarization was made more negative (Fig. 4*Ea*, open symbols), instead of increasing steadily; (2) at −15 to −55 mV, the current onset was not instantaneous but included a clearly gradual, time-dependent rising phase (Fig. 4*C*); and (3) the current decay was remarkably slow in a wide voltage window (see below, and Fig. 5). This notwithstanding, a close inspection of the current onset (Fig. 4*C*) clearly revealed the existence of two components: (i) an initial component that developed in an abrupt, nearly instantaneous fashion (Fig. 4*C*, wide arrowheads), followed by (ii) the gradually activating current. The distinction of the two components was particularly evident in a limited voltage window (−45 to −60 mV) in which component (ii) decreased in amplitude while maintaining relatively slow activation kinetics; in these cases, the two components were separated by a clear notch (Fig. 4*C*, narrow arrowheads), which indicates that component (i) is decaying as component (ii) is growing. Because the activating pulse at 0 mV also elicited a persistent Na^+-current component (Fig. 4*B*), the above observations suggest that component (i) represents the I_{NaP} tail current. To verify this possibility, it was necessary to directly compare the amplitude of component (i) with that of I_{NaP} at various voltages. To this aim, the maximal amplitude of component (i) was estimated by measuring, at each voltage, the average current amplitude over the time interval delimited by the two dotted vertical lines in Fig. 4*C*: this time interval corresponds to a sharp change in the current rising-phase slope, which converts into a relative minimum when the notch appears at lower voltages. The resulting *I–V* plot showed a linear behaviour over the whole voltage range explored (Fig. 4*D*, open symbols), with an extrapolated *x*-axis intercept at +72.0 mV. This value is not far from the predicted Na^+ equilibrium potential in our experiments (+86.7 mV). We also compared the voltage dependence of component (i) with that of I_{NaP}. As an estimate of I_{NaP} amplitude, we measured the sustained inward current at the end of the 100 ms repolarizing pulses following I_{NaR} decay (I_{end}) (Fig. 4*B*, horizontal bars). It can be seen in Fig. 4*D* that component (i) and I_{end} closely paralleled at −15 to −40 mV, a voltage window in which I_{NaP} activation reaches a plateau (see above, Fig. 3*C* and *D*). The slightly lower amplitude of I_{end} with respect to component (i) in this voltage range could be justified by I_{NaP} inactivation developing during the 100 ms depolarizing pulses (see

the data points of which were averaged to obtain a measure of current amplitude. *C*, *I–V* relationship (○) and plot of permeability as a function of V_{test} (●) for the average I_{NaP} (see *B*). Permeability values have been derived from current values as explained in the text. The dashed–dotted line is the best fitting obtained by applying a single Boltzmann function to permeability data points; fitting parameters are also specified. The continuous line has been derived from the same fitting function by converting permeability into current on the basis of the GHK equation. *D*, the current recorded in a representative GC (cell B3312), in control conditions and in the presence of 1 μM TTx, in response to the ramp depolarization illustrated in the upper part of the panel. *E*, TTx-sensitive, ramp-evoked currents in the same cell. The current shown in *Ea* has been obtained by subtraction from the two tracings of *D*. The current shown in *Eb*, also TTx-subtracted, was elicited by a voltage ramp twice less steep. Note that in the *x*-axis time values have been replaced by the corresponding potential values. *F*, plot of permeability as a function of voltage for the current illustrated in *Ea*. The ascending branch of the tracing has been best-fitted with a single Boltzmann function (smooth, white curve); fitting parameters are also specified.

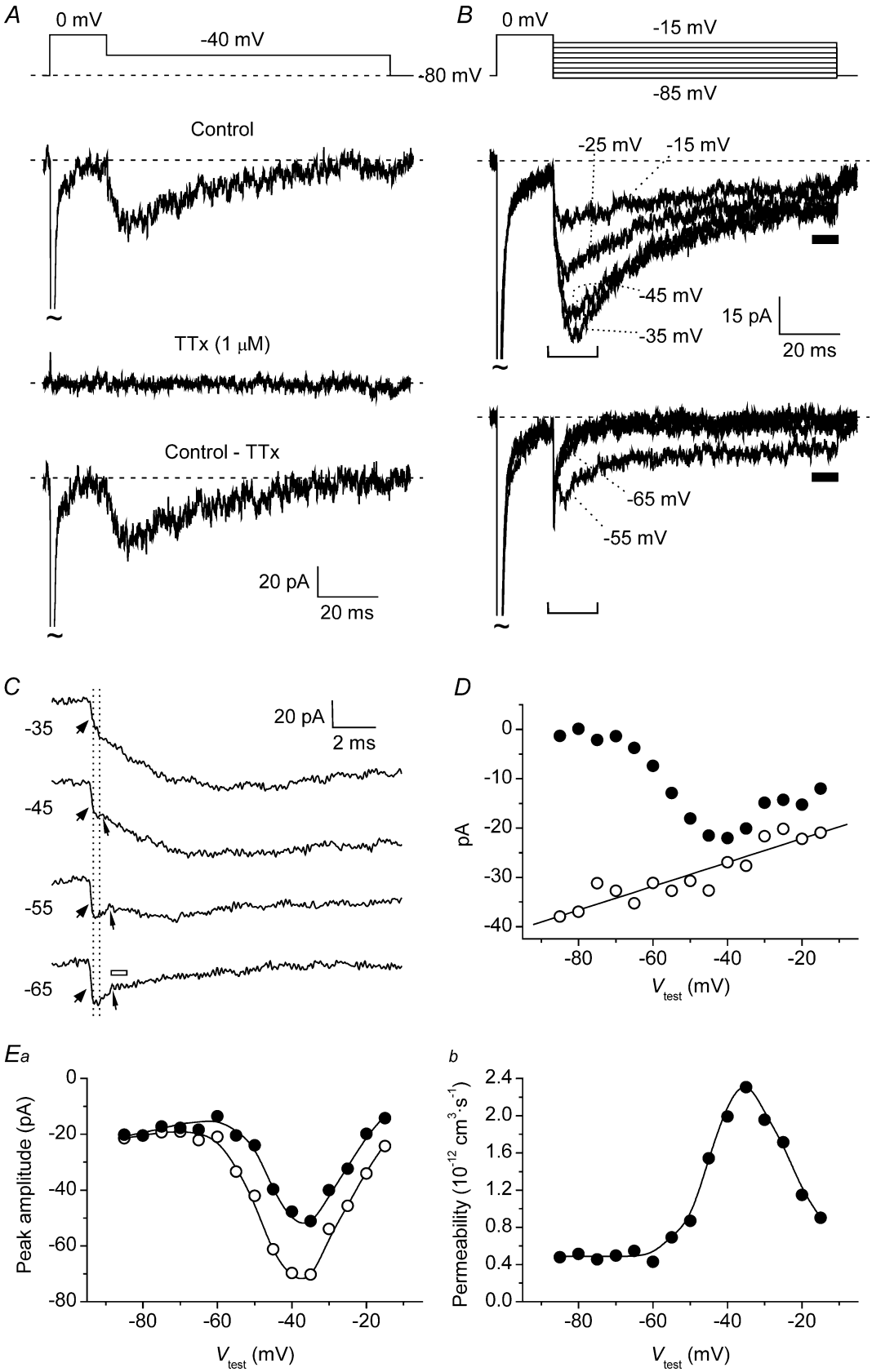

the second section of Results, and Magistretti & Alonso, 1999). These data are consistent with component (i) of repolarization-elicited current onset corresponding to an I_{NaP} tail current.

Clearly, it would be desirable to determine the amplitude of the current specifically identifiable as I_{NaR} in isolation from the underlying I_{NaP}. At −15 to −40 mV, where I_{NaP} activation is saturating, this could be conveniently done by subtracting I_{end} (as an approximate estimate of the steady I_{NaP} level) from peak current amplitude; indeed, at these potentials the establishment of a new, steady I_{NaP} level upon repolarization will be nearly instantaneous. At more negative voltages, in which a step repolarization will result in a new I_{NaP} level after I_{NaP}-tail relaxation, this can also be done under the assumption that I_{NaR} activation is slow enough as compared to I_{NaP}-tail decay. The 'net' I_{NaR} amplitude thus determined is plotted as a function of voltage in Fig. 4*Ea* (filled symbols). Current amplitude increased from −15 to −35 mV, where it showed a peak. At potentials negative to −35 mV, the current decreased back to reach, at about −60 mV, a non-zero level which then appeared to increase somewhat for further repolarizations. Note that at potentials negative to −55 mV, where I_{NaP} tail decay and I_{NaR} rising phase appeared to merge, I_{NaR} amplitude was obtained by considering the points that immediately followed a clear decrease in current–decay slope (see Fig. 4*C*, open bar), which presumably indicated I_{NaP}-tail subsiding. Permeability values were also calculated from 'net' I_{NaR} amplitude values and plotted as a function of voltage (Fig. 4*Eb*): the plot was bell-shaped with a maximum at −35 mV and a pedestal level at −60 to −85 mV corresponding to about 20% of the peak.

I_{NaR} kinetics was then analysed (Fig. 5). At −15 to −55 mV, I_{NaR} activation and decay could be described by a double exponential fitting function (Fig. 5*A*). Component (i) of the current's rising phase (see above) was excluded from fitting. At potentials negative to −55 mV, a single exponential function was used to describe I_{NaR} decay. The activation time constant (τ_{act}) showed a bell-shaped dependence on voltage, with a peak of about 2.75 ms at −35/−40 mV (Fig. 5*B*). The plot of time to peak (ttp) *versus* voltage also showed a similar bell-shaped behaviour (Fig. 5*C*). The decay time constant (τ_{dec}; Fig. 5*D*) ranged from 35 to 20 ms at −15 to −40 mV, and appeared to decrease steadily with increasingly negative potentials in this voltage window. τ_{dec} also fell abruptly at −35 mV (34 ms) to −60 mV (5 ms), whereas at −60 to −85 mV it maintained a rather constant value of about 5 ms.

I_{NaR} amplitude varied considerably among cells. A strong correlation was found between I_{NaR} maximal amplitude and the size of I_{NaT} (measured at the peak of the *I–V* relationship) (Fig. 6*A*), whereas no significant correlation was observed with the animal's age in the time window considered (16–23 postnatal days) (Fig. 6*B*). A subset of cells displayed no measurable, or extremely little, I_{NaR} component (Fig. 6*Ca*). Because these cells also showed relatively small I_{NaT} (<500 pA), and because of the prominent correlation between I_{NaR} and I_{NaT} sizes, it could be suspected that in these instances I_{NaR} amplitude simply fell below the threshold of detection. This was not the case, however, since clear I_{NaR} components could be unequivocally detected in other cells that expressed I_{NaT} of similarly low amplitude (Fig. 6*C* and *D*). The above findings suggest the existence of heterogeneity in GC expression of I_{NaR}. Such diversity in I_{NaR} expression

Figure 4. Resurgent Na^+ current (I_{NaR}) in GCs
A, I_{NaR} in a representative GC (cell D4206). The experimental tracings are the currents recorded, in control conditions and in the presence of 1 μM TTx, in response to the depolarizing-repolarizing voltage command shown in the top panel. The bottom tracing is the TTx-sensitive current obtained by subtraction. *B*, I_{NaR} tracings obtained by averaging the currents recorded in six different neurones. Eight selected tracings are shown; the corresponding voltage commands are illustrated in the upper part of the panel. *C*, four tracings from *B* are shown in an expanded time scale to provide a detail of I_{NaR} onset. The tracing region highlighted corresponds to that embraced by the square brackets in *B*. The wide arrowheads point to the initial phase of current development, characterized by an abrupt and clearly faster rise ('component (i)'). The narrow arrowheads point to the notch that may be observed between the initial phase and the late, slower phase of current development ('component (ii)'). The two dotted, vertical lines delimit the tracing region the points of which were averaged to obtain a measure of component-(i) peak amplitude. The open bar next to the lowermost tracing marks the region in which I_{NaR} amplitude was measured in those tracings in which, due to the absence of an identifiable I_{NaR} peak, component (i) and component (ii) were not clearly separated: note that the region chosen immediately follows an evident reduction of the current's decline speed, indicative of I_{NaP}-tail subsiding (see the text). *D*, *I–V* relationship of component-(i) peak amplitude (○) and of the sustained inward current observed at the end of the 100 ms repolarizing pulses after I_{NaR} decay (I_{end}; ●). Component-(i) peak amplitude was measured as illustrated in *C*. I_{end} amplitude was measured by averaging data points in the region marked by the horizontal bar in *B*. The straight line is the linear regression to component-(i) *I–V* plot, which returned an *x*-axis intercept at +71.7 mV, with *R* (regression coefficient) = 0.92, and *P* (the probability of *R* to be 0) $< 1 \times 10^{-4}$. *E*, voltage dependence of I_{NaR} peak amplitude and of the underlying permeability. *Ea*, the *I–V* relationship of raw I_{NaR} peak amplitude (○), and of 'net' I_{NaR} peak amplitude (●), obtained by subtracting I_{end} amplitude from raw I_{NaR} peak amplitude. *Eb*, the voltage dependence of the permeability underlying the 'net' I_{NaR}. Data points have been derived from those of *Ea* (●) by applying the GHK equation as described in Methods.

did not correlate with significant differences in I_{NaT} voltage dependence and kinetics. The half-activation potential ($V_{½}$) and slope factor (k) obtained from P_{NaT}–V plots averaged -30.9 ± 2.6 and -5.0 ± 0.6 mV, respectively, in I_{NaR}-lacking group 2 cells ($n = 3$), and -34.5 ± 3.1 and -4.5 0.6 mV, respectively, in group 2 cells in which I_{NaR} was present and greater than 15 pA in peak amplitude ($n = 4$; $P > 0.4$ in both cases). Moreover, in both groups, I_{NaT} kinetics was described by two exponential components with similar time constants.

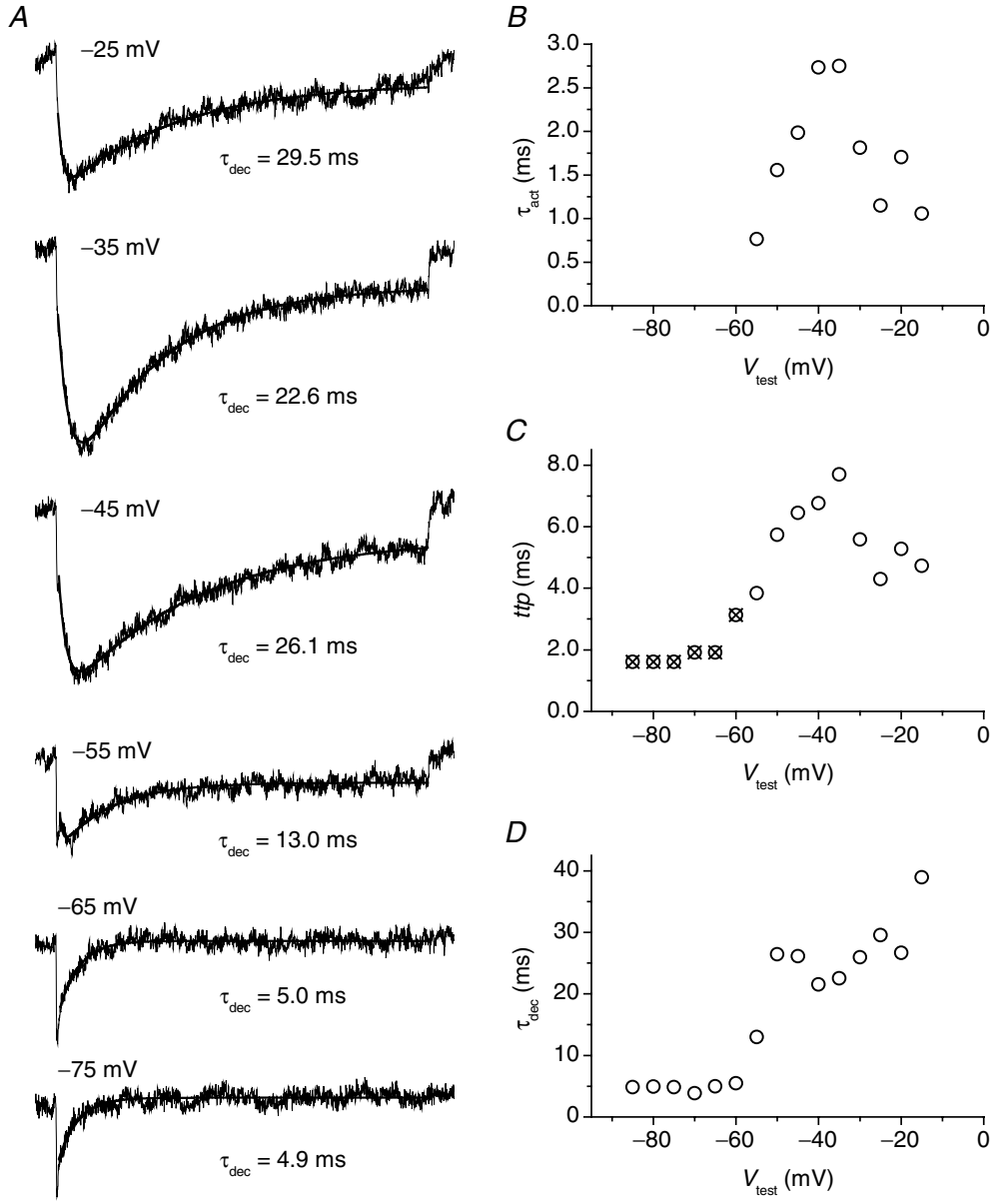

Figure 5. Kinetics of I_{NaR} activation and decay in GCs
A, average I_{NaR} tracings at six selected potentials. These tracings are taken from those shown in Fig. 4*B* (note that here only the tracing region corresponding to the repolarizing pulses is shown; the preceding part of the protocol has been omitted). The repolarization level is specified next to each tracing. Smooth lines are second- (tracings 1–4) or first- (tracings 5 and 6) order exponential fittings to the currents' time course. The time constant of the exponential component describing the current's decay (τ_{dec}) is also specified next to each tracing. *B*, plot of I_{NaR} activation time constant (τ_{act}) as a function of V_{test}. τ_{act} values were returned by the fittings illustrated in *A*, in those cases in which I_{NaR} development was separated and distinguishable from I_{NaP} tails. *C*, plot of I_{NaR} time-to-peak (ttp) as a function of V_{test}. ttp was calculated taking the repolarizing pulse's starting point as time zero. Open circles and crossed circles correspond to ttp values obtained from measurements made in the presence and in the absence, respectively, of a true I_{NaR} peak region. In the latter case, the 'peak' region to be considered was chosen as illustrated in Fig. 4*C* (lowermost tracing). *D*, plot of I_{NaR} decay time constant (τ_{dec}) as a function of V_{test}.

For instance, at −20 mV, decay time constants were 781.5 ± 115.2 μs and 6.46 ± 1.62 ms, and the relative A1 coefficient was 0.83 ± 0.05 in the former group ($n = 3$); and the same parameters averaged 691.4 ± 45.5 μs, 3.94 ± 1.13 ms, and 0.76 ± 0.02, respectively, in the latter group ($n = 4$; $P > 0.16$ in all cases). I_{NaP} peak amplitude relative to I_{NaT} peak amplitude was also not significantly different in I_{NaR}-lacking GCs (1.75 ± 0.71%, $n = 5$) and

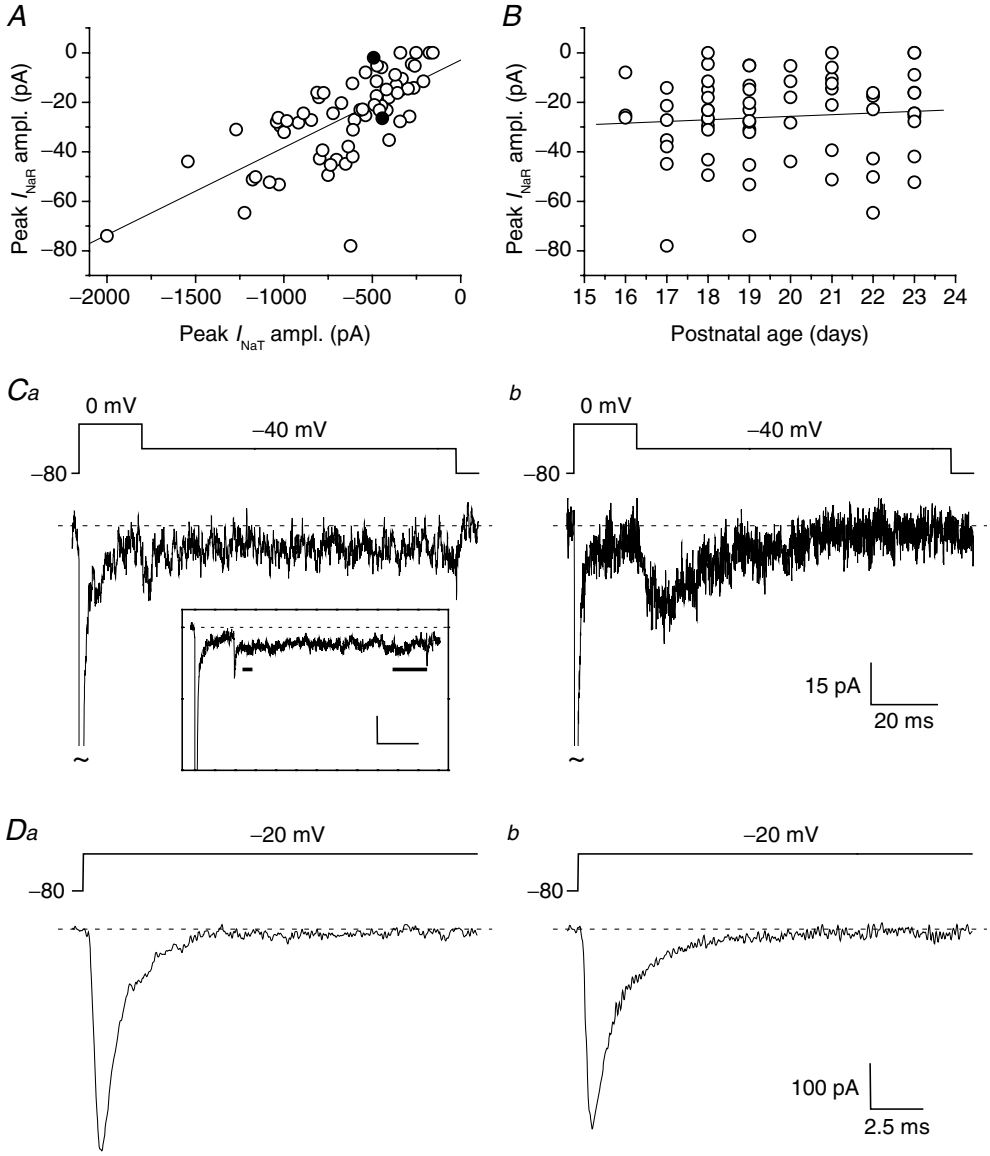

Figure 6. I_{NaR} amplitude strongly correlates with I_{NaT} amplitude, but I_{NaR} expression and amplitude also show intrinsic variability in GCs

A, scatter plot of I_{NaR} amplitude as a function of I_{NaT} amplitude. I_{NaR} and I_{NaT} amplitudes were measured at the peak of the respective *I–V* relationships (normally −40/−35 mV and −20 mV, respectively). The straight line is the linear regression to data points (slope factor = 35 pA nA^{-1}; $R = 0.69$, $P < 1 \times 10^{-4}$). *B*, scatter plot of I_{NaR} amplitude as a function of the postnatal age of the animal (in days after birth). The straight line is the linear regression to data points (slope factor = 0.51 pA day^{-1}; $R = 0.062$, $P = 0.62$). Data in *A* and *B* are from 67 cells. In both cases, I_{NaR} amplitude values are 'net' values, calculated as peak current minus I_{end} (see the text). *C* and *D*, I_{NaR} and I_{NaT}, respectively, recorded, at the peak of the *I–V* relationships, in two exemplary neurones (*Ca* and *Da*, cell B3428, representative of 7 cells; *Cb* and *Db*, cell B3327; both cells were classified as group 1 cells). Note the similar size of I_{NaT}, the presence of a clear I_{NaR} in *Cb*, and its almost complete absence in *Ca*. The two cells illustrated here are identified by the two filled symbols in *A*. *Ca*, inset, average tracing obtained from 7 cells (four group 1 cells, three group 2 cells) that were judged as devoid of a measurable I_{NaR} (same voltage protocol as in the main panel). Note that, at the time point at which an I_{NaR} peak would be expected (short horizontal bar), current amplitude was not different from that of the late I_{NaP} component (long horizontal bar). In the same 7 cells, the average I_{NaT} amplitude at the peak of the *I–V* relationship was −301.0 ± 47.0 pA. Calibration bars in the inset, 20 ms, 15 pA.

I_{NaR}-expressing GCs ($1.87 \pm 0.27\%$, $n = 14$; $P = 0.86$) (for this measure, only a subset of cells in which I_{NaT} peak amplitude was homogeneous and lower than 500 pA was considered for consistency).

Current-clamp recordings: depolarizing afterpotentials

To investigate the presence of functional correlates of I_{NaP} and/or I_{NaR} in GC intrinsic excitability, we carried out current-clamp experiments in which single APs were evoked with short (0.5 ms) depolarizing square current pulses. Baseline membrane potential (V_{bas}) was held at stationary levels in the -55 to -75 mV range by steady current injection, and 0.5 ms current steps were repeatedly applied at 1 Hz frequency. Step amplitude was regulated to obtain just above-threshold stimulation. Firing responses consisted in single spikes, evoked with a 1–5 ms delay from stimulus. In 4 out of 16 GCs, the AP terminated with a profound fast afterhyperpolarization (AHP) ($n = 2$) or with a quick return directly to V_{bas} ($n = 2$). In the remaining 12 cells, the AP fast repolarization phase was followed by an evident depolarizing afterpotential (DAP), making a hump 5–10 ms after spike peak. The hump consisted, in different cells, in either a true peak following a postspike relative minimum (Fig. 7*A* and *B*; $n = 10$), or an inflection in the membrane potential (V_m) trajectory after fast spike repolarization (Fig. 7*C*; $n = 2$).

We next examined whether the above-described DAPs could be underlain by I_{NaR} and/or I_{NaP}, or, alternatively, by other mechanisms, such as voltage-dependent Ca^{2+} currents. In two of the 12 cells, the DAP was prominent when resting potential was negative to -65 mV, but was markedly reduced by background depolarization (Fig. 7*Aa*). Moreover, in the same two cells the DAP was abolished by perfusion with a solution in which Ca^{2+} concentration was lowered to 0.5 mM and which contained 2 mM Ni^{2+} (Fig. 7*Ab*). These findings indicate that in a minority of GCs DAP generation depends on a Ca^{2+} current that requires hyperpolarization for repriming. In the remaining 10 GCs the DAP showed different properties. In all of these cells the DAP, either consisting in a true peak ($n = 8$) or in an inflection ($n = 2$), was reduced, rather that enhanced, by background hyperpolarization (Fig. 7*Ba* and *C*). In addition, in all cases tested, perfusion with the 0.5 mM Ca^{2+}, 2 mM Ni^{2+} solution reduced AP repolarization speed and largely abolished the relative minimum between the AP and the DAP, consistent with a role for Ca^{2+}-activated K^+ channels in AP repolarization (D'Angelo *et al.* 1998), but did not decrease the depolarization level reached during the DAP (Fig. 7*Bb*; $n = 5$ out of 5). Hence, in a majority of GCs the DAP is not generated by Ca^{2+} current(s) reprimed upon hyperpolarization. Other possible candidates that could account for DAP generation in GCs are I_{NaP} and I_{NaR}. In particular, due to its property of activating upon repolarization in a time-dependent manner, I_{NaR} appears particularly suitable to sustain a depolarization following AP repolarization. Slow perfusion with 200 nM TTx resulted in gradual, parallel reduction, and eventually suppression, of both the AP and the DAP ($n = 4$). Therefore, this approach did not allow us to establish whether the DAP depended on TTx-sensitive Na^+ channels or, rather, on the AP in itself. However, an indication about the nature of the DAP was provided by further analysis of its voltage dependence. In 6 out of 10 cells it was possible to regulate the level of the relative minimum between the AP and the DAP (V_{min}) by modifying the resting potential with steady current injection. In these cells, V_{min} varied in a voltage window comprised between -45 and -65 mV. If the DAP depends on I_{NaR} activation, its amplitude is expected to decrease as V_{min} is made increasingly negative, for two reasons: (i) with increasing hyperpolarization, I_{NaR} amplitude either decreases (at -45 to -60 mV) or remains relatively stable (negative to -60 mV), while its decay becomes progressively faster; and, simultaneously (ii) the negative current injected to hyperpolarize the cell counteracts positively going voltage deflections. Therefore, for the above six cells we plotted the difference between the absolute voltage level at DAP peak (V_{DAP}) and V_{min} as a function of V_{min}. In all cases, the difference $V_{DAP} - V_{min}$, which is an index of DAP amplitude, positively correlated with V_{min} (Fig. 7*D*). The slope coefficient returned by linear regression of these plots averaged 0.30 ± 0.06 mV mV^{-1}, and the correlation was statistically significant ($P < 0.003$ in all cases). Hence, in these cells the DAP was enhanced as the voltage relative minimum that preceded it was made more positive in the -65 to -45 mV voltage range. This behaviour is compatible with the properties of I_{NaR}.

Roles of I_{NaR} and I_{NaP}: computer modelling

To obtain further insight into the consequences of I_{NaR} and I_{NaP} expression on GC excitability, we resorted to computer modelling. Simulations were based on a previous single-compartment GC model (D'Angelo *et al.* 2001) implemented with the 13-state, allosteric Na^+-channel model by Raman & Bean (2001). This model, which generates I_{NaT}, I_{NaP} and I_{NaR} simultaneously, was re-parameterized to adequately reproduce the specific properties of GC VDNCs (see the Methods). Figure 8 illustrates the main properties of I_{NaT} and I_{NaR} returned, in simulated voltage-clamp experiments, by the model. The main properties of Na^+ currents were reproduced with good approximation. The voltage dependence of simulated I_{NaT} was very similar to that observed, on average, in experimental currents: the conductance-voltage plot

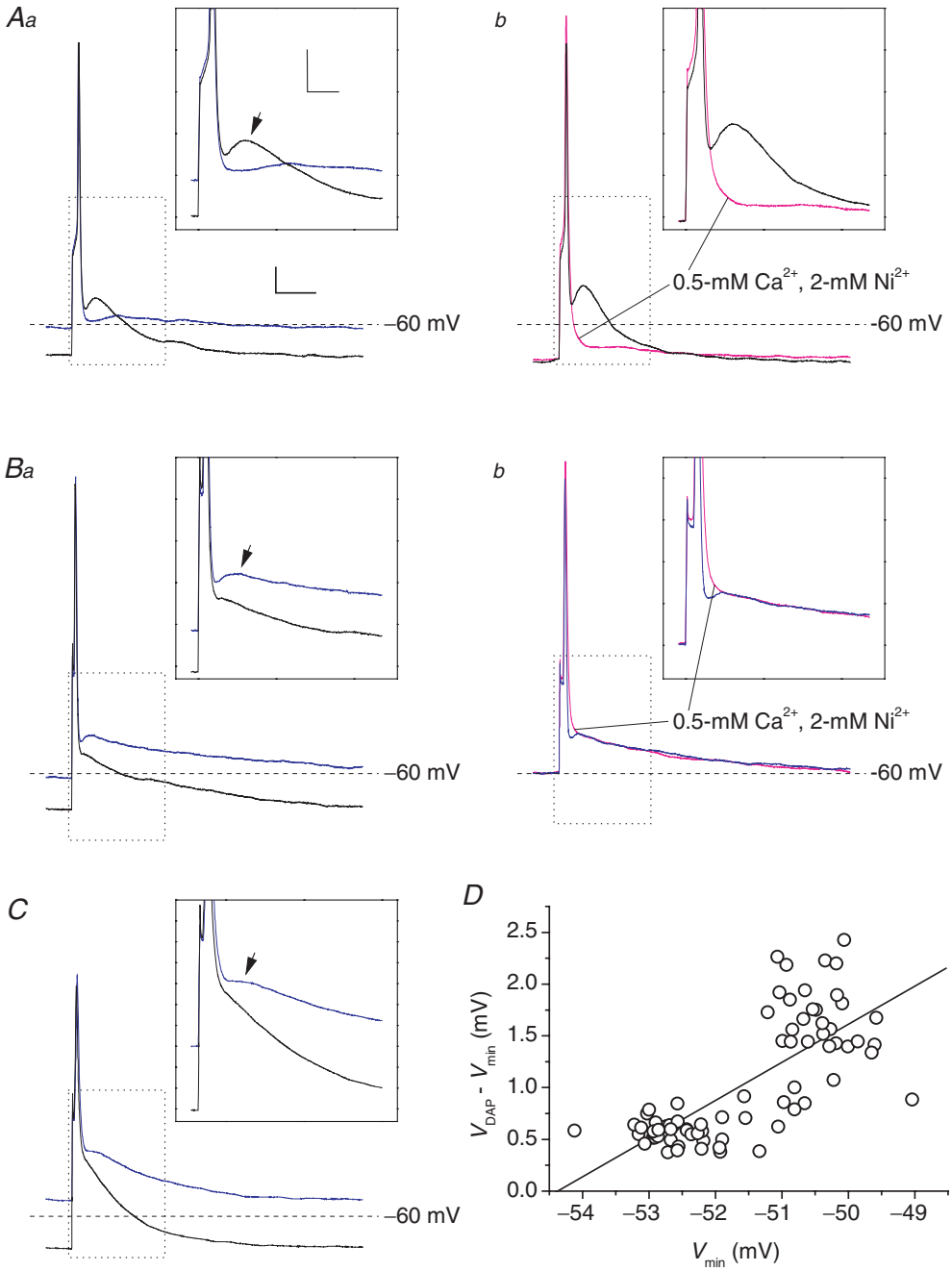

Figure 7. Depolarizing afterpotentials (DAPs) in GCs
A–*C*, APs evoked in three typical GCs (*A*, cell D5518, representative of 2 cells; *B*, cell A5516, representative of 8 cells; *C*, cell G100305a, representative of 2 cells) by 500 μs depolarizing square current pulses. *Aa*, *Ba* and *C* show APs recorded in each cell starting from two different baseline voltage levels (V_{bas}) (−70 mV, black tracings; and −55/−60 mV, blue tracings). *Ab* and *Bb*, APs recorded, starting from the same V_{bas}, under control conditions (black or blue tracings) and during perfusion with a solution containing 0.5 mM Ca^{2+} and 2 mM Ni^{2+} (tracings in magenta). Calibration bars: 25 ms, 8 mV. The insets show a detail of the tracings, corresponding to the region delimited by the dotted-line box, of each main panel. The arrows point to the DAPs following single APs. Calibration bars in insets: 10 ms, 10 mV. The amplitude of depolarizing current pulses varied from 0.28 (*Aa*) to 1.3 nA (*C*). *D*, plot of the difference between the absolute voltage level at DAP peak (V_{DAP}) and the level of the relative minimum between the AP and the DAP (V_{min}; see the text for details) as a function of V_{min} for the same cell illustrated in *B*. Each point corresponds to the measure made in an individual AP. The straight line is the linear regression to data points (slope coefficient = 0.368 mV mV^{-1}; $R = 0.74$, $P < 1 \times 10^{-4}$).

showed $V_{½}$ and k values of −28.9 mV and −5.4 mV, respectively (Fig. 8*Ab*; cf. Fig. 2*Bb*). The decay kinetics of simulated I_{NaT} closely approximated the fast decay component of experimental I_{NaT} (for instance, at 0 mV simulated I_{NaT} decayed monoexponentially with a time constant of 476.6 μs, to be compared with an average value of 431.1 μs for τ_{ina1} in experimental currents: cf. Fig. 2*Da*). Also, the properties of simulated I_{NaR} and I_{NaP}

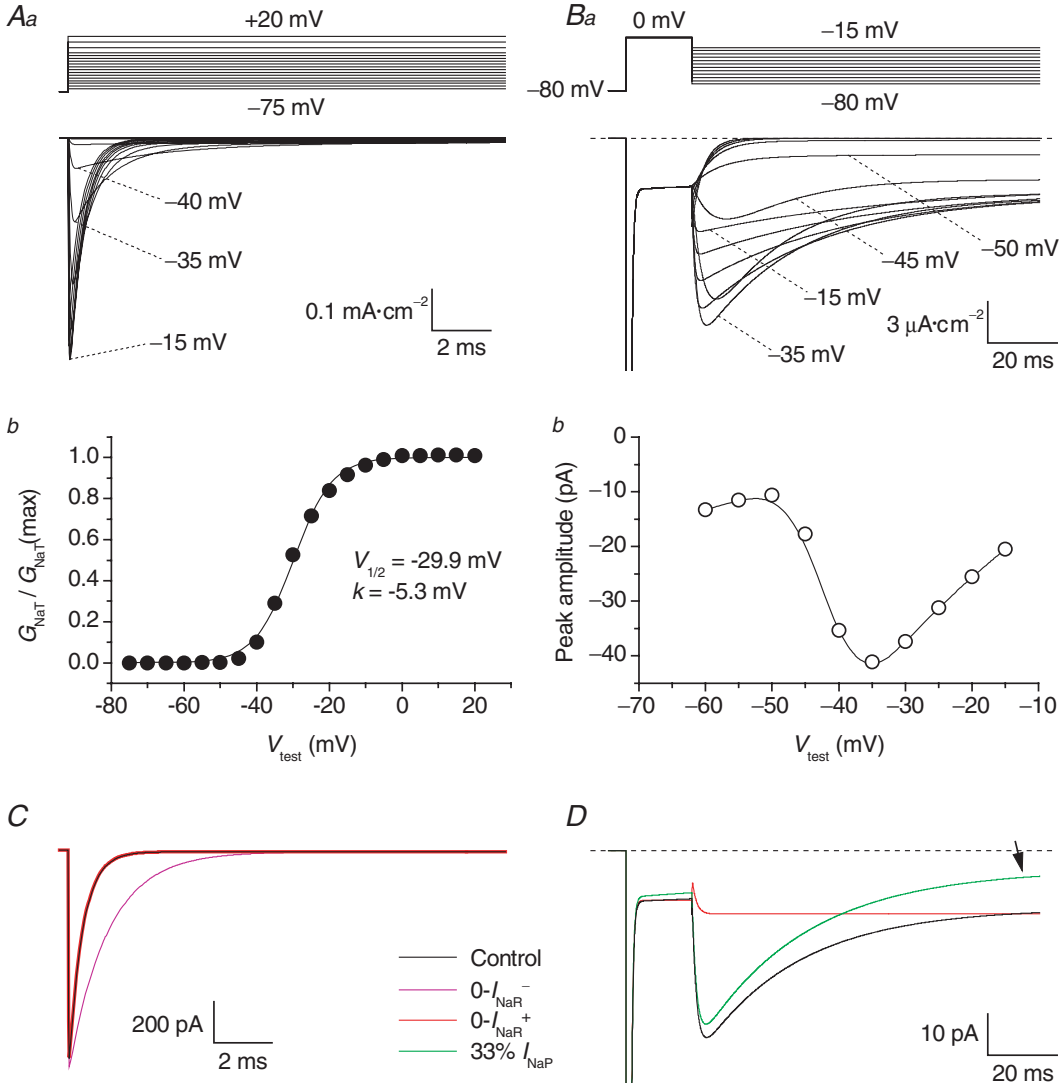

Figure 8. Simulated voltage-clamp activation of GC Na^+ currents
A, simulated I_{NaT}. *Aa*, the currents activated by a voltage-clamp protocol consisting of 15 ms depolarizing voltage steps at −70 to +20 mV in 5 mV increments, from a holding potential of −80 mV. Tracings corresponding to test potentials of −5, +5 and +15 mV have been omitted for clarity. The voltage-clamp protocol is schematized in the upper part of the panel. *Ab*, plot of normalized peak conductance ($\overline{G}_{NaT}$) as a function of test voltage. The plot has been fitted with a single Boltzmann function (continuous line). Fitting parameters are also specified. *B*, simulated I_{NaR}. *Ba*, currents activated by repolarizing pulses at −15 to −70 mV in −5 mV increments, after a 19 ms depolarizing step at 0 mV (the voltage-clamp protocol is schematized in the upper part of the panel). *Bb*, the *I–V* relationship of the simulated I_{NaR}. In all simulations, the integration step size was 0.4 μs. *C*, effects on I_{NaT} of manipulations on the kinetic scheme aimed at modifying I_{NaR}. Simulated currents evoked by 15 ms depolarizing steps at 0 mV are shown. The current obtained under control conditions is shown in black. The violet tracing is the current obtained after setting the rate constant of the O → OB reaction, ε, to 0 (0-I_{NaR}^- condition: see kinetic Scheme 1 and the text for details). The red tracing is the current after setting ε to 0, the rate constant of the O → I6 reaction, O_{on}, to 2.15 ms^{-1}, and the rate constant of the I6 → O reaction, O_{off}, to 0.01433 ms^{-1} (0-I_{NaR}^+ condition). Note that the black and the red tracings are almost completely indistinguishable. *D*, modifications of I_{NaP} and I_{NaR} obtained by variously manipulating the kinetic scheme. The black tracing is the simulated control current evoked by the protocol shown in *Ba* (with a return potential of −35 mV). The red tracing is the current obtained in the 0-I_{NaR}^+ condition (see above): note that I_{NaR} is abolished, whereas I_{NaP} is unmodified. The green tracing is the current obtained after setting O_{off} to 0.0015 ms^{-1}, and leaving all the other rate constants at their control settings: note that I_{NaP} is decreased at the steady state (arrow), whereas I_{NaR} is almost unaffected.

were reasonably close to those of experimental currents. Simulated I_{NaR} showed a peak in the *I–V* relationship at −35 mV, a monoexponential decay (with $\tau_{dec} = 29.3$ ms at −35 mV), and an abrupt acceleration of decay at −55 mV (Fig. 8*B*; cf. Figs 4*Ea* and 5*D*). Simulated I_{NaP} peaked at −35 mV, with a half-maximal activation potential of the underlying conductance of −48 mV (not shown). It should be noted that the model did not generate the slow component of I_{NaT} decay, suggesting that further kinetic details would be needed to fully reproduce the behaviours of real Na^+ channels.

The maximal specific Na^+ conductance ($\overline{G}_{Na}$) chosen for current-clamp simulations was 8 mS cm^{-2}, which yielded a peak Na^+-current density of −541.6 μA cm^{-2}. If one assumes Na^+ channels to be uniformly distributed on the somatic membrane, the latter value would correspond to a peak I_{NaT} amplitude of −957.1 pA (with a soma diameter of 7.5 μm), a value somewhat greater than those typically observed in real GCs (cf. Fig. 6*A*). However, Na^+-channel expression may be confined to more limited, highly excitable membrane subcompartments in GCs, including the axon initial segment (see Schaller & Caldwell, 2003). The ratios of I_{NaP} and I_{NaR} peak amplitudes to I_{NaT} peak amplitude were within the range of values observed in GCs (0.0078 and 0.026, respectively). With these settings, the model GC responded to injection of depolarizing current steps by firing regular trains of APs (Fig. 9*A* and *B*). AP frequency showed an approximately

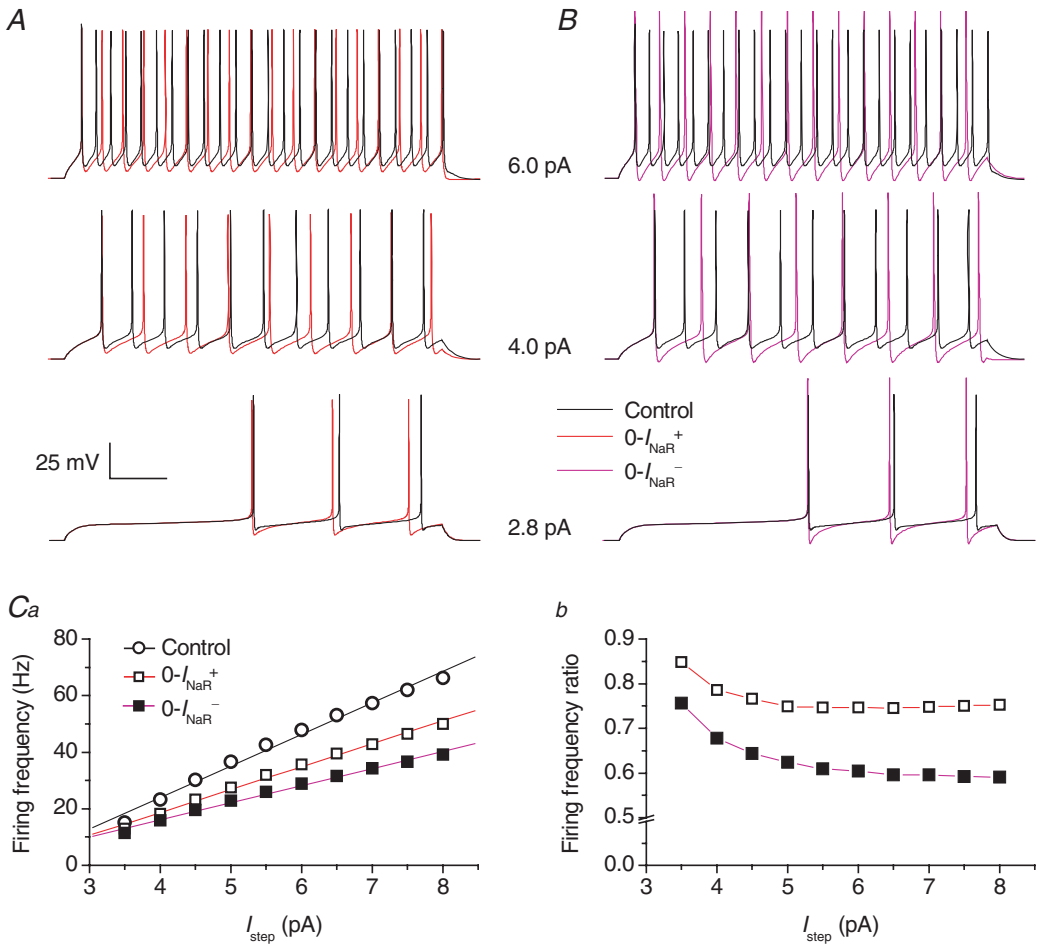

Figure 9. Effects of I_{NaR} on repetitive firing in a model of GC electrical activity
A and *B*, repetitive AP firing elicited by injection of 1 s (lower tracings) and 500 ms (middle and upper tracings) depolarizing current steps. Step current amplitude was 2.8 pA (lower tracings), 4 pA (middle tracings) and 6 pA (upper tracings). Black tracings are simulated voltage signals obtained under basal conditions. Red tracings (*A*) and violet tracings (*B*) were obtained after abolishing I_{NaR} by adopting the 0-I_{NaR}^+ condition settings, and the 0-I_{NaR}^- condition settings, respectively (see the text for details). The *x*-axis calibration bar is 150 ms for lower tracings, and 75 ms for middle and upper tracings. *Ca*, plot of firing frequency as a function of injected step current amplitude (I_{step}) (○, basal conditions; □, 0-I_{NaR}^+ condition; ■, 0-I_{NaR}^- condition). Straight lines are linear regression fittings to data points. Slope coefficients are 11.2 Hz pA^{-1} (○), 8.1 Hz pA^{-1} (□), and 6.0 Hz pA^{-1} (■). *Cb*, plot of the ratio of firing frequency in the 0-I_{NaR}^+ condition (□) and in the 0-I_{NaR}^- condition (■) to control firing frequency, as a function of stimulation intensity.

linear relationship with injected current amplitude, and the slope of the frequency–current plot (constructed for a stimulating-current range of 3.5–8.0 pA) was 11.2 Hz pA^{-1} (Fig. 9*Ca*). The apparent threshold for AP firing was at about −50 mV. All these properties are consistent with those experimentally observed for real GCs (D'Angelo *et al.* 1998).

We next examined the specific effects of I_{NaR} and I_{NaP} on AP firing. To do this, the two current components were manipulated separately as explained in Methods. In the 0-I_{NaR}^{+} condition, in which I_{NaR} is switched off with no changes in I_{NaT} kinetics, the frequency of tonic firing was reduced (Fig. 9*A*, red tracings), and the slope of the frequency–current plot decreased to 8.1 Hz pA^{-1} (Fig. 9*Ca*). The decrease in firing frequency was more marked at high stimulation levels (Fig. 9*Cb*), and maximal decrease was of about 25%. At just-threshold stimulation levels, AP firing was not impaired by the 0-I_{NaR}^{+} condition, and, instead, firing frequency was slightly increased (Fig. 9*A*, lower tracings), probably due to an enhancement of postspike AHP and, consequently, an acceleration of Na^{+}-channel recovery from activation. In the 0-I_{NaR}^{-} condition, in which I_{NaR} is suppressed by abolishing the O → OB transition with no compensation for I_{NaT} inactivation slowdown (see Methods), the changes in AP repetitive firing were similar to those observed in the 0-I_{NaR}^{+} condition, but more pronounced. The slope of the frequency–current plot further decreased to 6.0 Hz pA^{-1} (Fig. 9*Ca*). The maximal decrease in firing frequency, here again observed at high stimulation levels (Fig. 9*Cb*), was about 40%. The more prominent effects of the 0-I_{NaR}^{-} condition, as compared with the 0-I_{NaR}^{+} condition, on tonic firing, are probably the consequence of a markedly enhanced postspike AHP (Fig. 9*B*; see also below), which more effectively opposes the stimulating current in the interspike period.

I_{NaP} was modified by decreasing the rate constant of the I6 → O transition, O_{off} (see Methods). This change reduced the steady-state I_{NaP} component while negligibly affecting I_{NaT} and I_{NaR} (Fig. 8*D*). Decreasing the steady-state I_{NaP} by 58 to 67% impaired AP generation at just-threshold stimulation levels (Fig. 10*A*, lower

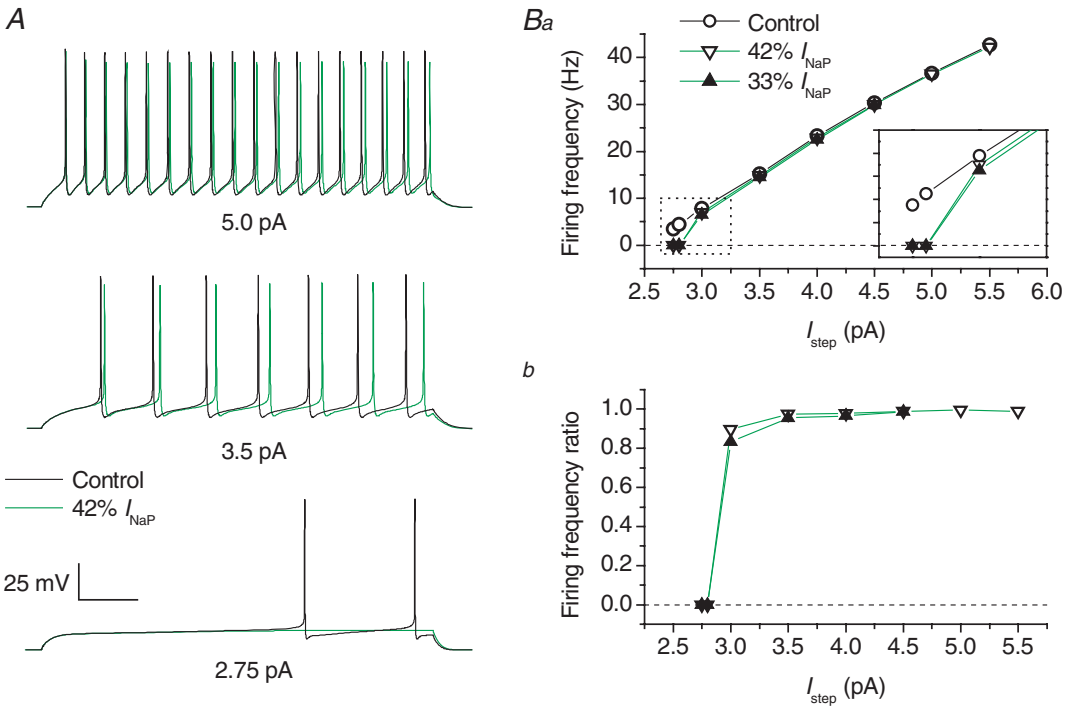

Figure 10. Effects of I_{NaP} on repetitive firing in model GCs
A, AP firing elicited by 1 s (lower tracings) and 500 ms (middle and upper tracings) depolarizing current steps. Step current amplitude was 2.75 pA (lower tracings), 3.5 pA (middle tracings) and 5 pA (upper tracings). Black tracings correspond to basal conditions, green tracings to a 58% reduction of the steady-state I_{NaP} component obtained by lowering the rate constant, O_{off} (see Scheme 1 and the text for details) to 40% of its control value. The *x*-axis calibration bar is 150 ms for lower tracings and 75 ms for middle and upper tracings. *Ba*, plot of firing frequency as a function of I_{step} for basal conditions (○), for 58% reduction of I_{NaP} (▽), and for 67% reduction of I_{NaP} (▼). A detail of the plot at low stimulation intensities (dotted-line box) is highlighted in the inset (each *y*-axis division is 2 Hz). *Bb*, plot of the ratio of firing frequency after 58% (▽) or 67% (▼) I_{NaP} reduction to control firing frequency, as a function of stimulation intensity.

tracings). The frequency of repetitive firing was moderately affected at slightly above-threshold stimulation levels, and very little at still higher stimulation levels (Fig. 10*A*, middle and upper tracings; Fig. 10*Ba* and *Bb*). It should be noted that in the 13-state Na^+-channel model, the I_{NaP} reduction obtained by lowering O_{off} is less prominent at early times of sustained depolarizations than at the steady state (see Fig. 8*D*). This is a consequence of slow release of channels from the OB state to the O state during sustained depolarization. Therefore, lowering O_{off} could have little effect on the amplitude of the I_{NaP} fraction activated during short interspike periods, and this could limit the significance of the above observation that reducing I_{NaP} by lowering O_{off} has little influence on tonic high-frequency firing. However, we also verified the effect of lowering O_{off} after abolishing the transitions to the OB state (0-I_{NaR}^+ condition above), a situation in which I_{NaP} amplitude is equally decreased at the steady state and at earlier times (Supplemental Fig. B, panel A). Again, we found that I_{NaP} reduction markedly affects AP firing at just-threshold stimulation levels, but has no major effects on high-frequency tonic firing (Supplemental Fig. B, panels B and C).

Finally, we tested the ability of the model to reproduce DAPs. Single APs triggered by simulated injection of 0.5 ms depolarizing current pulses under basal conditions were followed by small but clear DAPs (Fig. 11). Starting from a V_{bas} of −65 mV, the DAP consisted in a true peak following

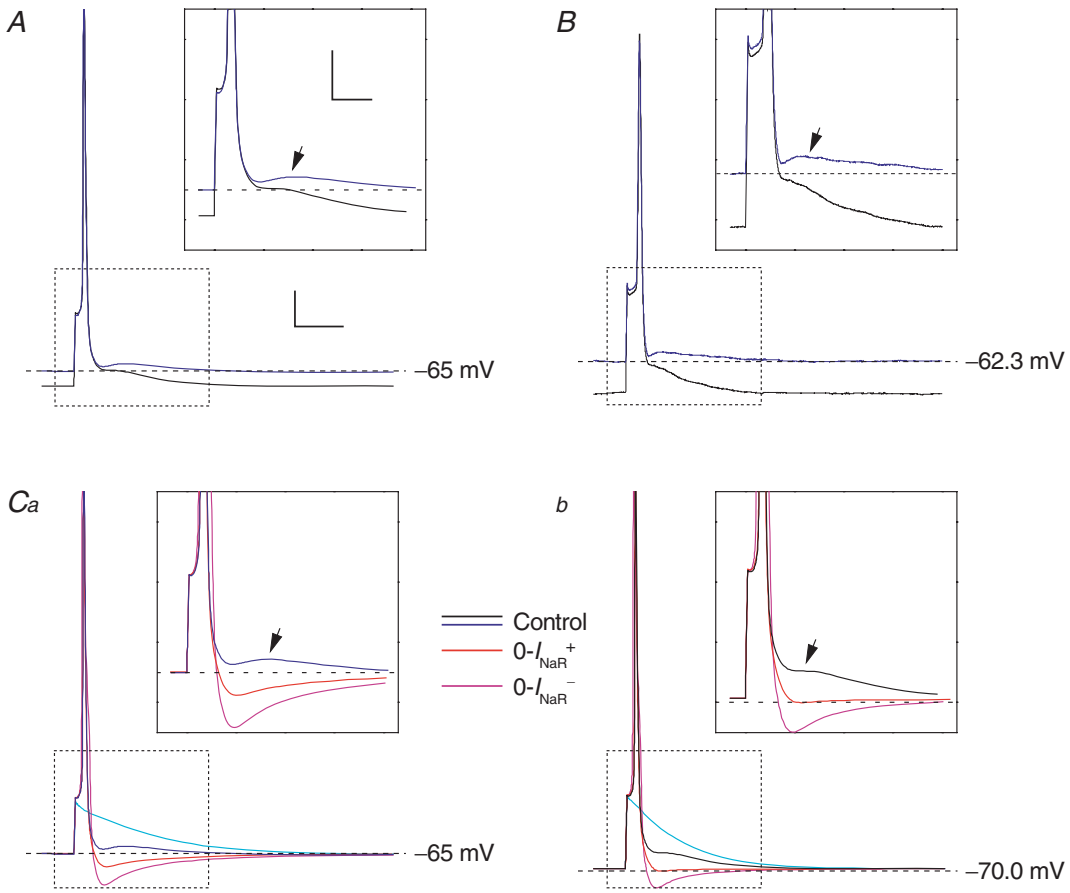

Figure 11. I_{NaR} determines DAP generation in model GCs
Each panel shows single APs evoked by injection of 0.5 ms, above-threshold square current pulses. In all panels, black and blue tracings were obtained, under basal (control) conditions, from a V_{bas} of −70/−71 mV and −65/−62 mV, respectively. Insets show a detail of the tracings corresponding to the region delimited by the dotted-line box in each main panel, and arrows point to the DAPs that follow APs. *A*, simulated APs obtained from V_{bas} of either −70 or −65 mV under basal conditions are shown superimposed. *B*, single APs and DAPs evoked in a real GC (cell C5518) from V_{bas} of either ∼−62 or ∼−71 mV: note the similarity with the results of computer simulations (*A*). *C*, effect of I_{NaR} suppression obtained by adopting the 0-I_{NaR}^+ condition settings (red tracings) or the 0-I_{NaR}^- condition settings (violet tracings) at V_{bas} of −65 (*Ca*) and −70 mV (*Cb*). Light blue tracings represent passive responses to just-subthreshold stimuli. The amplitude of depolarizing current pulses was 106–108 pA (V_{bas}, −65 mV) or 135–137 pA (V_{bas}, −70 mV) in all simulated experiments. Calibration bars for main panels, 15 ms, 10 mV. Calibration bars for insets, 8 ms, 8 mV.

a postspike relative minimum (Fig. 11*A*, blue tracing). Starting from a more negative V_{bas} (−70 mV), the DAP consisted in a simple inflection (Fig. 11*A*, black tracing). The maximal, absolute level reached during the DAP was more positive starting from −65 mV than from −70 mV (−63 *versus* −65 mV) (Fig. 11*A*). These properties of the DAP closely resemble those of DAPs experimentally recorded in GCs (compare *A* with *B* in Fig. 11). The 0-I_{NaR}^{+} condition abolished the DAP (Fig. 11*C*, red tracings), which was replaced by a prompt return to baseline when V_{bas} was −70 mV (Fig. 11*Cb*), or a fast AHP at more positive V_{bas} (Fig. 11*Ca*). These findings indicate that I_{NaR} is necessary for DAP generation. In the 0-I_{NaR}^{-} condition, AP amplitude and duration were increased due to slowed Na^+-channel inactivation. As a consequence, the post-spike AHP was further augmented, due to enhanced activation of repolarizing K^+ currents (Fig. 11*C*, violet tracings).

Discussion

The present study provides a detailed biophysical and functional characterization of voltage-dependent Na^+ currents, comprising I_{NaT}, I_{NaP} and I_{NaR}, in cerebellar GCs *in situ*. The electrophysiological measurements were favoured by the unusually compact electrotonic structure of GCs, which allowed for a precise kinetic analysis of Na^+ currents. GCs, like other cerebellar neurones, present complex near-threshold behaviours, to which Na^+ currents have been proposed to give a critical contribution (D'Angelo *et al.* 1998, 2001). Our experiments and simulations support a significant role for I_{NaP} in priming AP initiation during near-threshold stimulation, and for I_{NaR} in boosting the efficiency of repetitive firing and in generating DAPs. The latter effect may be important to explain the tendency of GCs to discharge in bursts and repetitive AP sequences *in vivo* (Chadderton *et al.* 2004).

Properties of I_{NaT}

The major problem affecting Na^+ current recordings in neurones *in situ* is the voltage-clamp escape caused by remote localization of Na^+ channels in the dendrites and axon. Although GCs are among the most electrotonically compact neurones (Silver *et al.* 1992; D'Angelo *et al.* 1993, 1995), in most cells we could not fully prevent clamp problems possibly arising from incomplete space-clamp control and Na^+-channel expression in neuronal processes. In some GCs, however, I_{NaT} consisted of a well-clamped component only, suggesting that in these cells only channels located in a membrane region electrotonically proximal to the soma were contributing to the recorded current. In such cases, I_{NaT} showed the voltage dependence and fast kinetics typical of classical neuronal Na^+ currents. In particular, I_{NaT} voltage dependence was similar to that observed in cultured GCs (Osorio *et al.* 2005) in the presence of reverted Na^+ gradient to render Na^+ currents non-regenerative and prevent local escape from clamp. To describe the kinetic properties of GC I_{NaT}, we tentatively applied a classical HH formalism. However, this approach was limited by the fact that proper fitting of I_{NaT} kinetics required the n exponent to increase with membrane potential (from ∼2 at −45 mV to ∼9 at +10 mV). This finding is anomalous but not surprising, since it is well known that the HH model does not reflect the real mechanisms of Na^+-channel state transitions. I_{NaT} inactivation was biexponential, with one time constant in the 4–0.4 ms range and the other in the 10 ms–1 ms range. Biexponential I_{NaT} decay has also been observed in other central neurones (Huguenard *et al.* 1988; Sah *et al.* 1988; Gähwiler & Llano, 1989; Park & Ahmed, 1991; Cummins *et al.* 1994).

Properties of I_{NaP}

The persistent Na^+ current, I_{NaP}, is widely present in central neurones, but its biophysical properties show some variability in activation threshold, relative amplitude compared to I_{NaT}, and slow inactivation. In GCs, the permeability underlying I_{NaP} was half-maximally activated at −55 mV, i.e. 25 mV more negative than I_{NaT}, and a maximal, steady level was reached at −40 to −15 mV. The voltage range of GC I_{NaP} activation (−60 to −30 mV) overlapped with the region of Na^+-dependent inward rectification in the steady-state *V–I* plot obtained from current-clamp experiments (D'Angelo *et al.* 1998; see below). The peak amplitude of the I_{NaP} evoked with long-lasting depolarizing step pulses averaged about −9 pA and represented 1.5–2% of I_{NaT} peak amplitude. It should be noted that these values could be slightly overestimated, because channel expression in neuronal processes may cause spurious increases in the amplitude of steady-state inward currents under voltage-clamp conditions (White *et al.* 1995). However, no marked distortion in current voltage dependence is expected (White *et al.* 1995). I_{NaP} expression has also been reported for cultured GCs (Osorio *et al.* 2005). In that case, channels responsible for I_{NaP} were located in neuronal processes, and I_{NaP} peak amplitude was greater than in GCs *in situ* (∼20 pA), which could reflect the prominent process development typical of GC cultures. We also observed that when I_{NaP} was evoked with slow depolarizing ramps, its amplitude decreased as depolarization rate was reduced. In other neurones (Fleidervish & Gutnick, 1996; Magistretti & Alonso, 1999; Agrawal *et al.* 2001) this behaviour has been related to the existence of a slow voltage-dependent I_{NaP} inactivation that proceeds on a time scale of seconds.

Biophysical properties and possible molecular correlates of I_{NaR}

Perhaps the most intriguing property of GC Na^+ currents is the expression of a resurgent component, I_{NaR} (Magistretti *et al.* 2004; Afshari *et al.* 2004). The biophysical properties of GC I_{NaR} were similar to those observed in Purkinje cells and other neurones (Raman & Bean, 1997; Do & Bean, 2003; Cummins *et al.* 2005), and included a bell-shaped voltage dependence with a peak at −35 mV, and a marked voltage dependence of activation and decay kinetics, both of which showed an abrupt acceleration at potentials negative to −40/−45 mV.

To account for I_{NaT}, I_{NaP} and I_{NaR} in Purkinje cells, Raman & Bean (2001) developed a 13-state allosteric model with five closed states, one open state, six inactivated states, and a 'blocked' state accessed from the open state (see Scheme 1). This model implicitly assumes that a single Na^+ channel is endowed with states explaining a multiplicity of kinetic behaviours. In the model, I_{NaP} is determined by the equilibrium between open, inactivated, and blocked states. I_{NaR} is generated by release of channels from the blocked to the open state. Blocking is determined by an intracellular 'blocking particle' competing with the classical 'inactivating ball' for binding to the open channel. Binding of the blocking particle is voltage independent, whereas unbinding is strongly voltage dependent, probably as an indirect consequence of inwardly directed Na^+ flow inside the channel upon repolarization (through a mechanism of displacement due to electrostatic repulsion, or mechanical momentum, or both). By preventing the inactivating ball from binding to open channels, the blocking particle would therefore create, upon depolarization, a 'reservoir' of non-inactivated channels that would be exploited in repolarization to produce a transient inward current. The relative proportions, voltage dependence, and kinetics of I_{NaT}, I_{NaP} and I_{NaR} in GCs could all be accounted for by the Raman & Bean (2001) model. A more precise correspondence of modelling with experimental currents may require parameterization of the kinetic scheme through the application of specific fitting algorithms (e.g. Vanier & Bower, 1999), and additional data from single-channel recordings.

In Purkinje cells, the presence of I_{NaR} has been related to the expression of Na_v 1.6 Na^+ channels (Raman *et al.* 1997) as a necessary, although not sufficient (Pan & Beam, 1999), requirement. Na^+ channel α subunits different from Na_v 1.6 (Do & Bean, 2003), including Na_v 1.2 (Rush *et al.* 2005), have then been shown to also provide a possible molecular substrate for I_{NaR} in other neurones. GCs do express Na_v 1.6 and Na_v 1.2 mRNA and protein at high levels (Schaller & Caldwell, 2003). More recently, a tight correlation between I_{NaR} expression and the Na^+-channel auxiliary β4 subunit (Grieco *et al.* 2005) has been established. Indeed, a portion of the β4 subunit cytoplasmic tail can act as the 'blocking particle' which, according to the Raman-Bean model, competes with the classical 'inactivating ball' for binding to the channel's open state. Unlike Purkinje cells, however, GCs do not show high expression levels of β4 subunit mRNA and protein in *in situ* hybridization and immunohistochemical tests (Yu *et al.* 2003). Although this does not rule out the presence of functional β4 subunits, it may indicate that molecules other than the β4 subunit determine I_{NaR} in GCs.

Roles of I_{NaP} and I_{NaR}

The impact of a given membrane current on neuronal electrogenesis depends on the specific electrotonic structure and the channel complement of the neurone in which the current is expressed. In some neurones, I_{NaP} is relatively large (hundreds of pA) and determines processes like oscillations and spike priming (discussed in Magistretti & Alonso, 2002). In GCs, I_{NaP} has small amplitude, yet it can have a major impact on membrane excitability due to the small size of these neurones and their high input resistance. Indeed, an inward current of 9 pA (the average, peak I_{NaP} amplitude we observed in GCs) would produce an 18 mV depolarization on a resistance of 2 GΩ (the average GC input resistance at −70 mV, under physiological ionic conditions: D'Angelo *et al.* 1995, 1998; Brickley *et al.* 1996). The fact that the voltage range of GC I_{NaP} activation (−60 to −30 mV) overlapped with the region of Na^+-dependent steady-state inward rectification observed under current-clamp conditions supports the prediction that a persistent Na^+ current critically influences GC near-threshold excitability and the rate at which GC membrane potential approaches firing threshold (D'Angelo *et al.* 1998). Accordingly, our computer simulations indicated that I_{NaP} has a critical influence in promoting AP firing at low, just-threshold levels of stimulation, whereas the impact of I_{NaP} on high-frequency firing was much smaller. I_{NaP} has also been shown to sustain subthreshold membrane potential oscillations and to amplify GC resonance in the theta-frequency range (D'Angelo, 2001).

Because of its property of activating in repolarization after depolarizations able to activate and inactivate I_{NaT}, I_{NaR} is more suitable to provide a depolarizing drive following firing of single APs, or during repetitive discharge. The response of Purkinje cells to brief, just-threshold depolarizing pulses, which in most other neurones would trigger single APs, consists in the discharge of doublets or triplets of APs (Raman & Bean, 1997). I_{NaR} has been proposed to underlie this firing pattern (Raman & Bean, 1997). In GCs, we found that single APs are most frequently followed by evident DAPs that, in ∼80% of cases, show features compatible with a role of I_{NaR} in their generation. Computer modelling confirmed that I_{NaR} expression at levels similar to those

frequently observed experimentally results in generation of DAPs closely resembling real DAPs. DAPs produced by GCs did not trigger discharge of AP doublets or triplets (except in a single case, data not shown). However, during injection of just-threshold depolarizing steady currents, GC firing is frequently characterized by spike clustering (D'Angelo *et al.* 1998, 2001). I_{NaR}-dependent DAPs could contribute to this behaviour, as well as to oscillatory burst firing occurring during partial inhibition of K^+ currents (D'Angelo *et al.* 1998). It was recently reported that antidromic stimulation of parallel fibres by brief electrical shocks applied to the molecular layer results in doublets or triplets of APs at the GC soma (Isope *et al.* 2004), and it was concluded that this behaviour is a consequence of intrinsic excitable properties of GCs. Although the mechanism of spike repetition during antidromic stimulation remains to be established, it is possible that I_{NaR} contributes to its generation.

Our results also indicate the existence of marked variability in I_{NaR} amplitude among GCs expressing transient Na^+ currents of similar size. At the same time, a fraction of GCs did not produce DAPs, and in another cell subset DAPs were generated by a Ca^{2+}-, hyperpolarization-dependent mechanism not involving I_{NaR}. It could thus be hypothesized that heterogeneity in I_{NaR} expression is a critical factor in determining the variable ability of GCs to generate DAPs at resting potential.

How general the role of I_{NaR} could be in sustaining DAPs in central neurones is still unexplored. Hippocampal CA1 pyramidal neurones have been found to generate DAPs sensitive to TTx (Jensen *et al.* 1996; Azouz *et al.* 1996), that were attributed to I_{NaP} action. At the time of those reports, however, the existence of I_{NaR} was not known. In principle, therefore, I_{NaR} may conceivably contribute to DAP generation also in CA1 neurones. On the other hand, preliminary data suggest that CA1 pyramidal neurones *in situ* do not express I_{NaR} (J. Magistretti and L. Castelli, unpublished results), making a role of I_{NaP} still possible. It is worth remarking that, although the results of our modelling strongly suggest that I_{NaR} is necessary for DAP generation in cerebellar GCs, they do not rule out a possible contribution of I_{NaP} to the overall depolarization. Indeed, in the kinetic model we adopted for Na^+-current simulation, I_{NaP} is but an aspect of a global Na^+ current, and it is not possible to suppress its early phases unless I_{NaR} is also abolished. In fact, I_{NaP} generation could imply more specialized mechanisms (including modal gating and long-lived burst openings: Alzheimer *et al.* 1993; Magistretti & Alonso, 2002; Magistretti *et al.* 2003) that would make it less strictly interconnected with other Na^+ current components.

The results of our computer simulations also indicated that an additional functional consequence of I_{NaR} expression in GCs is an increase in firing frequency during sustained depolarization and in the gain of the frequency–stimulation relationship. This is in agreement with what has been found for Purkinje cells (Khaliq *et al.* 2003). The influence of I_{NaR} on firing frequency was maximal in the presence of high stimulation levels, and minimal or absent at near-threshold stimulation levels. This behaviour is opposite to that found for I_{NaP}. Therefore, I_{NaP} and I_{NaR} appear to provide cerebellar GCs with two complementary mechanisms for promoting AP firing at different levels of activity.

Distribution of I_{NaR} and implications for cerebellar function

I_{NaR} is a Na^+ current of recent identification. In addition to GCs (this study; Afshari *et al.* 2004), I_{NaR} is expressed in other important cerebellar neurones, including Purkinje cells, where it has been originally described (Raman & Bean, 1997), cerebellar unipolar brush cells (Mossadeghi & Slater, 1998; Afshari *et al.* 2004), and neurones of deep cerebellar nuclei (Raman *et al.* 2000; Afshari *et al.* 2004). Preliminary results indicate that I_{NaR} is also present in Golgi cells (J. Magistretti and E. D'Angelo, unpublished data). Being present in five major cerebellar neuronal types, I_{NaR} may thus be particularly important for cerebellar function. Subthreshold, persistent Na^+ currents also have a well-characterized role in setting the excitable properties of Purkinje cells (Llinás & Sugimori, 1980; Raman & Bean, 1999), as well as in GC and Golgi cell functions (D'Angelo *et al.* 1998, 2001; Forti *et al.* 2004). What is the reason for expressing such specific Na^+-current components in so many cerebellar neuronal types? A possible interpretation, based on the role attributed to I_{NaR} and/or I_{NaP} in AP conglomeration and bursting (Franceschetti *et al.* 1995; Raman & Bean, 1997; Parri & Crunelli, 1998; Brumberg *et al.* 2000), is that the cerebellum privileges spike bursts to communicate, and that this coding property must be maintained throughout the circuit by distributed mechanisms like those provided by I_{NaR} and I_{NaP}. GCs are known to produce spike bursts following punctate tactile stimulation (Chadderton *et al.* 2004), and Purkinje and deep cerebellar nuclei cells also have the ability of conglomerating spikes by exploiting I_{NaR} (Raman & Bean, 1997; Afshari *et al.* 2004). Spike bursts are also important for eliciting parallel fibre–Purkinje cell long-term depression (LTD) (Casado *et al.* 2002). Unfortunately, there is currently no means to inhibit I_{NaR} or I_{NaP} selectively in order to directly test their role in cerebellar physiology. Specific network models may help understanding the emergence of I_{NaR} and I_{NaP} effects on cerebellar network computation.

References

Afshari FS, Ptak K, Khaliq ZM, Grieco TM, Slater NT, McCrimmon DR & Raman IM (2004). Resurgent Na^+ currents in four classes of neurons of the cerebellum. *J Neurophysiol* **92**, 2831–2843.

Agrawal N, Hamam BM, Magistretti J, Alonso A & Ragsdale DS (2001). Persistent sodium channel activity mediates subthreshold membrane potential oscillations and low-threshold spikes in entorhinal cortex layer V neurons. *Neuroscience* **102**, 53–64.

Alzheimer C, Schwindt PC & Crill WE (1993). Modal gating of Na^+ channels as a mechanism of persistent Na^+ current in pyramidal neurons from rat and cat sensorimotor cortex. *J Neurosci* **13**, 660–673.

Azouz R, Jensen MS & Yaari Y (1996). Ionic basis of spike after-depolarization and burst generation in adult rat hippocampal CA1 pyramidal cells. *J Physiol* **492**, 211–223.

Brickley SG, Cull-Candy SG & Farrant M (1996). Development of a tonic form of synaptic inhibition in rat cerebellar granule cells resulting from persistent activation of $GABA_A$ receptors. *J Physiol* **497**, 753–759.

Brumberg JC, Nowak LG & McCormick DA (2000). Ionic mechanisms underlying repetitive high-frequency burst firing in supragranular cortical neurons. *J Neurosci* **20**, 4829–4843.

Casado M, Isope P & Ascher P (2002). Involvement of presynaptic *N*-methyl-D-aspartate receptors in cerebellar long-term depression. *Neuron* **33**, 123–130.

Chadderton P, Margrie TW & Hausser M (2004). Integration of quanta in cerebellar granule cells during sensory processing. *Nature* **428**, 856–860.

Cummins TR, Dib-Hajj SD, Herzog RI & Waxman SG (2005). Nav1.6 channels generate resurgent sodium currents in spinal sensory neurons. *FEBS Lett* **579**, 2166–2170.

Cummins TR, Xia Y & Haddad GG (1994). Functional properties of rat and human neocortical voltage-sensitive sodium currents. *J Neurophysiol* **71**, 1052–1064.

D'Angelo E, De Filippi G, Rossi P & Taglietti V (1995). Synaptic excitation of individual rat cerebellar granule cells *in situ*: evidence for the role of NMDA receptors. *J Physiol* **484**, 397–413.

D'Angelo E, De Filippi G, Rossi P & Taglietti V (1998). Ionic mechanism of electroresponsiveness in cerebellar granule cells implicates the action of a persistent sodium current. *J Neurophysiol* **80**, 493–503.

D'Angelo E, Nieus T, Maffei A, Armano S, Rossi P, Taglietti V, Fontana A & Naldi G (2001). Theta-frequency bursting and resonance in cerebellar granule cells: experimental evidence and modeling of a slow K^+-dependent mechanism. *J Neurosci* **21**, 759–770.

D'Angelo E, Rossi P & Taglietti V (1993). Different proportions of *N*-methyl-D-aspartate and non-*N*-methyl-D-aspartate receptor currents at the mossy fibre-granule cell synapse of developing rat cerebellum. *Neuroscience* **53**, 121–130.

Do MT & Bean BP (2003). Subthreshold sodium currents and pacemaking of subthalamic neurons: modulation by slow inactivation. *Neuron* **39**, 109–120.

Eccles JC, Ito M & Szentágothai J (1967). *The Cerebellum as a Neuronal Machine*. Springer, Berlin.

Fleidervish IA & Gutnick MJ (1996). Kinetics of slow inactivation of persistent sodium current in layer V neurons of mouse neocortical slices. *J Neurophysiol* **76**, 2125–2130.

Forti L, Mapelli J, Cesana E & D'Angelo E (2004). Ionic mechanisms of autorhythmic firing and intrinsic electroresponsiveness in rat cerebellar Golgi cells. *FENS Abstracts* **2**, 492, A222.8.

Franceschetti S, Guatteo E, Panzica F, Sancini G, Wanke E & Avanzini G (1995). Ionic mechanisms underlying burst firing in pyramidal neurons: intracellular study in rat sensorimotor cortex. *Brain Res* **696**, 127–139.

Gähwiler BH & Llano I (1989). Sodium and potassium conductances in somatic membranes of rat Purkinje cells from organotypic cerebellar cultures. *J Physiol* **417**, 105–122.

Grieco TM, Malhotra JD, Chen C, Isom LL & Raman IM (2005). Open-channel block by the cytoplasmic tail of sodium channel 4 as a mechanism for resurgent sodium current. *Neuron* **45**, 233–244.

Hines ML & Carnevale NT (1997). The NEURON simulation environment. *Neural Comput* **9**, 1179–1209.

Huguenard JR, Hamill OP & Prince DA (1988). Developmental changes in Na^+ conductances in rat neocortical neurons: appearance of a slowly inactivating component. *J Neurophysiol* **59**, 778–795.

Isope P, Franconville R, Barbour B & Ascher P (2004). Repetitive firing of rat cerebellar parallel fibres after a single stimulation. *J Physiol* **554**, 829–839.

Jensen MS, Azouz R & Yaari Y (1996). Spike after-depolarization and burst generation in adult rat hippocampal CA1 pyramidal cells. *J Physiol* **492**, 199–210.

Khaliq ZM, Gouwens NW & Raman IM (2003). The contribution of resurgent sodium current to high-frequency firing in Purkinje neurons: an experimental and modeling study. *J Neurosci* **23**, 4899–4912.

Llinás R & Sugimori M (1980). Electrophysiological properties of *in vitro* Purkinje cell somata in mammalian cerebellar slices. *J Physiol* **305**, 171–195.

Magistretti J & Alonso A (1999). Biophysical properties and slow-voltage dependent inactivation of a sustained sodium current in entorhinal cortex layer-II principal neurons: a whole-cell and single-channel study. *J Gen Physiol* **114**, 491–509.

Magistretti J & Alonso A (2002). Fine gating properties of channels responsible for persistent sodium current generation in entorhinal cortex neurons. *J Gen Physiol* **120**, 855–873.

Magistretti J, Castelli L & D'Angelo E (2004). Three functionally different types of voltage-dependent Na^+ currents in rat cerebellar granule cells in situ. *FENS Abstracts* **2**, 412, A187.7.

Magistretti J, Ragsdale DS & Alonso A (2003). Kinetic diversity of single-channel burst openings underlying persistent Na^+ current in entorhinal cortex neurons. *Biophys J* **85**, 3019–3034.

Mossadeghi B & Slater NT (1998). Persistent and resurgent sodium currents in cerebellar unipolar brush cells. *Society for Neuroscience Abstracts* **24**, 1078.

Osorio N, Alcaraz G, Padilla F, Couraud F, Delmas P & Crest M (2005). Differential targeting and functional specialization of sodium channels in cultured cerebellar granule cells. *J Physiol* **569**, 801–816.

Pan F & Beam KG (1999). The absence of resurgent sodium current in mouse spinal neurons. *Brain Res* **849**, 162–168.

Park CC & Ahmed Z (1991). Characterization of sodium current in developing rat diencephalic neurons in serum-free culture. *J Neurophysiol* **65**, 1011–1021.

Parri HR & Crunelli V (1998). Sodium current in rat and cat thalamocortical neurons: role of a non-inactivating component in tonic and burst firing. *J Neurosci* **18**, 854–867.

Raman IM & Bean BP (1997). Resurgent sodium current and action potential formation in dissociated cerebellar Purkinje neurons. *J Neurosci* **17**, 4517–4526.

Raman IM & Bean BP (1999). Ionic currents underlying spontaneous action potentials in isolated cerebellar Purkinje neurons. *J Neurosci* **19**, 1663–1674.

Raman IM & Bean BP (2001). Inactivation and recovery of sodium currents in cerebellar Purkinje neurons: evidence for two mechanisms. *Biophys J* **80**, 729–737.

Raman IM, Gustafson AE & Padgett D (2000). Ionic currents and spontaneous firing in neurons isolated from the cerebellar nuclei. *J Neurosci* **20**, 9004–9016.

Raman IM, Sprunger LK, Meisler MH & Bean BP (1997). Altered subthreshold sodium currents and disrupted firing patterns in Purkinje neurons of Scn8a mutant mice. *Neuron* **19**, 881–891.

Rush AM, Dib-Hajj SD & Waxman SG (2005). Electrophysiological properties of two axonal sodium channels, Nav1.2 and Nav1.6, expressed in mouse spinal sensory neurones. *J Physiol* **564**, 803–815.

Sah P, Gibb AJ & Gage PW (1988). The sodium current underlying action potentials in guinea pig hippocampal CA1 neurons. *J Gen Physiol* **91**, 373–398.

Schaller KL & Caldwell JH (2003). Expression and distribution of voltage-gated sodium channels in the cerebellum. *Cerebellum* **2**, 2–9.

Silver RA, Traynelis SF & Cull-Candy SG (1992). Rapid-time-course miniature and evoked excitatory currents at cerebellar synapses *in situ*. *Nature* **355**, 163–166.

Vanier MC & Bower JM (1999). A comparative survey of automated parameter-search methods for compartmental neural models. *J Comput Neurosci* **7**, 149–171.

Yu FH, Westenbroek RE, Silos-Santiago I, McCormick KA, Lawson D, Ge P, Ferriera H, Lilly J, DiStefano PS, Catterall WA, Scheuer T & Curtis R (2003). Sodium channel 4, a new disulfide-linked auxiliary subunit with similarity to 2. *J Neurosci* **23**, 7577–7585.

White JA, Sekar NS & Kay AR (1995). Errors in persistent inward currents generated by space-clamp errors: a modeling study. *J Neurophysiol* **73**, 2369–2377.

Acknowledgements

We thank Dr Thierry Nieus for helpful assistance in implementation of Na^+-current model. This study was supported by FIRB grant no. RBAU01JRCF from the Italian Ministry of Education, University and Research (MIUR) to J.M., by EU grants IST-2001–35271 and QLG3-CT-2001-02256 to E.D., and by FIRB grant no. RBNE01AAS7 to E.D. L.C. was supported by a fellowship from MIUR (PRIN grant no. 2003060538 to J.M.).

Supplemental material

The online version of this paper can be accessed at:
DOI: 10.1113/jphysiol.2006.106682
http://jp.physoc.org/cgi/content/full/jphysiol.2006.106682/DC1
and contains supplemental material consisting of two figures:

Supplemental Figure A. Hodgkin-Huxley (HH) fitting of I_{NaT} activation.

Supplemental Figure B. Effects of manipulations aimed at reducing I_{NaP} before and after abolishment of I_{NaR} in computer simulations.

This material can also be found as part of the full-text HTML version available from http://www.blackwell-synergy.com